# Efficient Uncertainty Quantification for Marine CSEM via Swi-DREI: A Physics-Driven Deep Reparameterization Ensemble Approach with Implicit Regularization

Hao Liang[1,3], Changchun Yin[1]*, Zhanxiang He[2], Bo Zhang[1], Yunhe Liu[1], Xiuyan Ren[1], Yang Su[1], Thomas Hermans[3]

1. College of Geo-exploration Science and Technology, Jilin University, Changchun, China

2. Advanced Institute for Ocean Research, Southern University of Science and Technology, Shenzhen, China

3. Department of Geology, Ghent University, Ghent, Belgium

* Corresponding author: Changchun Yin

E-mail address: yinchangchun@jlu.edu.cn

ORCID (Hao Liang): 0000-0003-4423-3562

This manuscript is a nonpeer-reviewed preprint submitted to EarthArXiv. It is currently under consideration for publication in *Geophysical Journal International*.

**Abstract**

Marine controlled-source electromagnetic (MCSEM) method serves as a pivotal geophysical tool for characterizing deep-sea hydrocarbon reservoirs or gas hydrates. However, restricted by the exponential decay of EM fields in conductive media and the spatial incompleteness of data acquisition systems, the inverse problem faces challenges of severe non-linearity and non-uniqueness. This study develops a Swish-Gated Linear Units (SwiGLU) based deep reparameterization ensemble Inversion framework, designated as Swi-DREI, for accelerated uncertainty quantification. By exploiting the implicit structural regularization in deep neural networks, the framework successfully resolves geological backgrounds and sharpens the boundaries of anomalies without requiring external training datasets. To efficiently map complex multi-modal posterior distributions, a parallelized deep ensemble strategy is executed, combined with a statistical selection scheme based on clustering and interface probabilities to eliminate the boundary blurring typical of conventional arithmetic averaging. Numerical experiments demonstrate that the proposed framework possesses significant advantages in delineating high-resistivity thin layers, maintaining robustness under challenging scenarios with 20% Gaussian noise and 45% missing data. Applications to field data further verify the practical feasibility of the proposed approach. The results indicate that the proposed method can successfully reconstruct high-resolution resistivity profiles matching actual geological sequences while providing quantitative risk assessments for target identification. This framework establishes a rigorous, training data-free paradigm for interpreting complex marine CSEM data and balances high-resolution physical imaging with high-confidence uncertainty evaluation.

**Keywords:** Marine Controlled source electromagnetics (CSEM); Deep learning; Deep reparameterization; Uncertainty Quantification.

## 1. Introduction

Marine controlled-source electromagnetic (MCSEM) methods, as a geophysical exploration technology with high sensitivity to seabed electrical structures, are widely used in oil, gas hydrate, and mineral resource exploration, as well as mid-ocean ridge and upper mantle tectonic

studies (Constable 2010; Key 2012; Guo et al. 2020; Grayver 2024). A conventional frequency-domain EM system consists primarily of a towed low-frequency horizontal electric dipole used as a transmitter and multiple receivers deployed on the seafloor. During operations, the towed transmitter supplies power directly into the seawater, while the seafloor receivers record signals propagating through and reflected by the seabed anomalies. Consequently, the seafloor electrical structure can be reconstructed by processing and inverting the recorded EM data. Although MCSEM data exhibits good detection capabilities to high-resistivity anomalies, the inversion and interpretation process still faces severe challenges with non-linearity and ill-posedness.

To counteract the challenges in electromagnetic inverse problems, deterministic formulations prioritize the integration of explicit a priori characteristics—such as spatial smoothness or structural sparsity—into the objective function via a regularization term. The mathematical configuration of this regularization fundamentally governs the geometric properties of the solution space: traditional L2-norm smoothing guarantees convergence stability but blurs sharp geoelectrical interfaces, as exemplified by classical smooth-constrained inversions (Constable et al. 1987; Key 2009, 2016), whereas L1-norm (Su et al. 2022; Liu et al. 2024) or Total Variation (TV) (Rudin et al. 1992; Wang and Yu 2024) constraints improve boundary definition at the risk of generating non-physical staircase artifacts. To obtain the final model, the minimization of this regularized functional is executed via standard gradient-based iterative solvers, such as the non-linear conjugate gradient (NLCG), Gauss-Newton (GN), or limited-memory Broyden-Fletcher-Goldfarb-Shanno (L-BFGS) algorithms (Li et al. 2026a). Ultimately, these deterministic point estimates remain heavily dependent upon the selection of the initial model, rendering the optimization susceptible to trapping within local minima while providing either no uncertainty quantification or merely limited evaluations restricted to linearized error propagation, precluding a comprehensive characterization of subsurface uncertainty (Zhdanov 2010).

The application of machine learning to geophysical inverse problems provides an effective path to address the bottlenecks of traditional inversion approaches (Yu and Ma 2021; Huang et

al. 2026). The data-driven deep learning inversions leverage the powerful non-linear fitting capacity of deep neural networks to learn the non-linear mappings between the data space and the model space using extensive training datasets. Upon completion of model training, the inference delivers imaging in few seconds, demonstrating significant advantages in handling complex non-linear features. In addition, this class of methods generally maintains low dependence on initial models and exhibits a certain degree of capability for global optimization. However, the end-to-end deep learning inversions suffer frequently from "black-box" characteristics and lack strict constraints from physical equations (Michel et al., 2022). More critically, the performance of data-driven paradigms depends on the scale and representativeness of the training database. When processing field data that contain unknown noise or unseen geological structures, the out-of-distribution (OOD) generalization issues frequently occur (Wang et al. 2022; Ahmed et al., 2024). To overcome the limitations of data-driven approaches, the physics-driven deep learning has emerged (Raissi et al. 2019; Karniadakis et al. 2021). This technique incorporates physical equations into the training process of the neural network to ensure that the network remains constrained by physical laws while learning non-linear mappings, thereby yielding inverted models compliant with physical principles. Without significantly increasing computational costs, the physical constraints effectively enhance inversion performance, the generalization capability of the model, and the robustness. Currently, integrating physics-driven methods with deep learning has become a major research focus in geophysical exploration. Fig. 1 illustrates the workflows for data-driven, physics-driven, and deep reparameterization inversions within the deep learning framework.

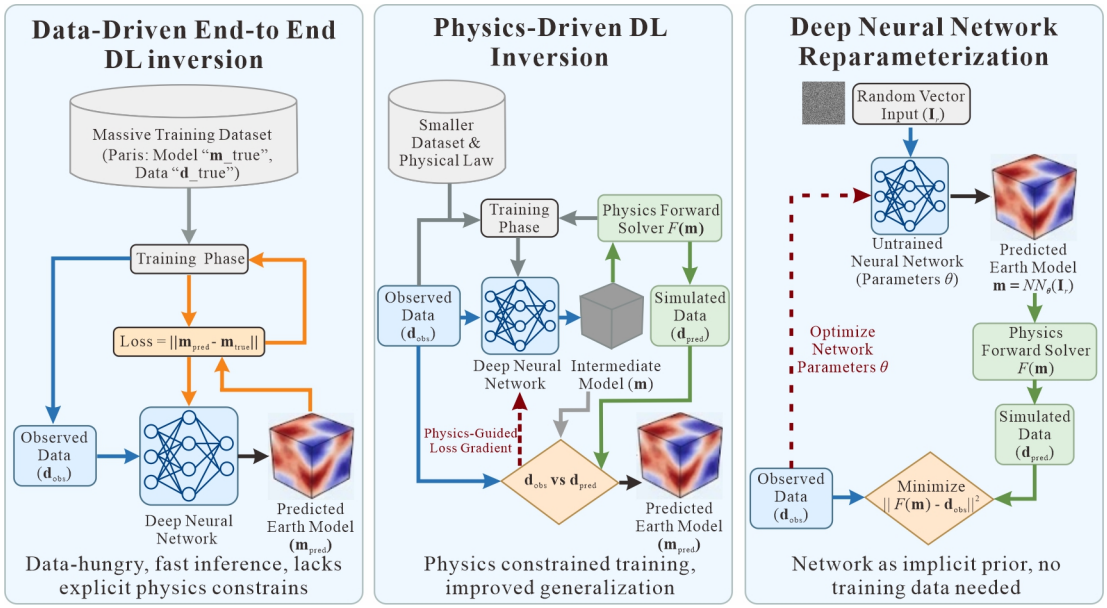



**Figure. 1** Schematic diagram of deep learning inversion workflows. The left panel shows the end-to-end data-driven inversion, the middle panel shows the physics-driven inversion that incorporates physical law constraints, while the right panel shows the physics-guided deep reparameterization inversion.

As a key branch of the physics-driven paradigm, the deep reparameterization techniques (Ulyanov et al. 2018) leverage the implicit representation of neural networks to map model parameters into a low-dimensional latent space. This parameterization strategy alleviates the non-linearity of the objective function while incorporating a learnable regularization mechanism into the optimization process. Existing literature indicates that this methodology has been successfully applied to the construction of prior constraints that effectively mitigate the dependence on initial models in the inversion and suppress crosstalk among multiple physical parameters. For instance, He and Wang (2021) adopted a two-step training scheme based on multilayer convolutional neural networks that first pre-train the network to map random vectors to an initial seismic velocity model and subsequently utilize the gradients derived from the forward modeling for physics-constrained optimization. Similarly, Zhu et al. (2022) employed shallow convolutional architectures to generate velocity model perturbations for superposition onto a background model, and demonstrated substantial robustness in synthetic tests contaminated with random Gaussian noise. To solve the problem with dependence on the initial model, Sun et al. (2023) proposed an implicit full-waveform inversion

framework that employs multi-layer perceptrons to directly establish the mapping between spatial coordinates and subsurface velocity fields. In multi-parameter scenarios, Dhara and Sen (2022) developed an autoencoder-based collaborative framework that compresses seismic records into a latent space via an encoder and subsequently generates perturbations of distinct physical parameters through parallel decoders. Liu et al. (2026a) implemented a backbone-branch network design and achieved the prediction of multiple physical properties by sharing core network features among sub-networks. Additionally, Lopez-Alvis et al., (2022) using convolutional neural network to reparamterize complex geometries with sharp interface for gradient-based inversion for ground penetrating radar (GPR). Hansen and Finlay (2022) developed a sampling-free probabilistic inversion method that minimizes a negative log-likelihood loss to directly estimate posterior statistics from observed electromagnetic data, completely circumventing the need for explicit posterior realizations. Guo et al. (2025) introduced a U-Net-based joint inversion framework for magnetotelluric, seismic, and gravity data that utilizes global features to autonomously establish correlations among different physical attributes and yields inverted models with high structural consistency and varying spatial resolutions. A review of these developments reveals that while deep reparameterization has been widely deployed in the seismic exploration, the application of this approach to EM methods remains relatively limited. Furthermore, the current mainstream frameworks mostly provide a single inverted model, whereas the uncertainty quantification in geophysical inverse problems is of crucial importance for evaluating non-uniqueness and mitigating the risks associated with subsequent geological interpretation.

Although probabilistic inversion via the Bayesian paradigm, such as Markov chain Monte Carlo (McMC), provides rigorous posterior distributions (Tarantola 2005; Sen and Stoffa 2013; Liu et al. 2026b), the required millions of forward simulations (Mosegaard and Tarantola 1995) render it computationally prohibitive for multidimensional or trans-dimensional MCSEM problems (Minsley 2011; Buland and Kolbjørnsen 2012; Ray and Key 2012). As a surrogate, Monte Carlo Dropout (MCD) approximates variational inference (Gal and Ghahramani 2016), yet its restricted distribution family tends to collapse into a single local extremum, thereby

underestimating uncertainty in multi-modal, highly non-linear model spaces (Osband et al. 2016; Folgoc et al. 2021). Furthermore, conventional Variational Inference (VI), which utilizes explicit analytical distributions like the mean-field Gaussian (Blei et al. 2017), theoretically conflicts with the implicit regularization and spectral bias of network reparameterization (Rahaman et al. 2018; Ulyanov et al. 2018; Xu et al. 2019). Forcing VI requires ungrounded weight space priors (Wenzel et al. 2020), while its mean-field assumption destroys the topological correlation among parameters (Cheng et al. 2019, Izmailov et al. 2021). Therefore, a new strategy capable of both preserving the benefits of implicit structural regularization and efficiently quantifying the multi-modal posterior distribution is urgently required.

As an effective non-Bayesian approximate inference approach, deep ensembles demonstrate outstanding performance in uncertainty quantification and generalization (Lakshminarayanan et al. 2017; Ovadia et al. 2019). Unlike variational inference, this parallel optimization strategy is highly compatible with untrained neural network reparameterization, fully preserving implicit regularization effects while driving individual models to cross loss barriers and converge into distinct optimal regions within the multi-modal MCSEM objective function space (Fort et al. 2019). To leverage these capabilities, this study introduces a training data-free, physics-driven deep reparameterization ensemble inversion framework designated as Swi-DREI. By executing parallel optimization runs constrained directly by the Maxwell equations, the proposed scheme captures diverse local optimal models to quantify uncertainty at a lower computational expense than conventional sampling. The efficacy of the Swi-DREI framework is subsequently validated through synthetic benchmarks featuring complex salt domes and thin hydrocarbon reservoirs, followed by an application to an MCSEM field survey dataset for deep-sea geological interpretation.

## 2. Methodology

To introduce the methodology of the proposed inversion framework, we will first briefly review the conventional MCSEM inversion method. After that, we will formulate the deep reparameterization framework to transform the optimization problem from the model space to the network parameter space, thereby leveraging the implicit regularization effects inherent in

deep neural networks. Then we introduce three strategies on how to incorporate the prior geological information through reference-guided models. Finally, we deploy the deep ensemble strategy to characterize the multi-modal posterior distribution, coupled with a joint selection mechanism that combines unsupervised clustering and interface probability to mitigate the issue with boundary blurring.

### 2.1 MCSEM Inversion

The conventional MCSEM inversion is a purely physics-driven approach that utilizes gradient-based optimization to reconstruct subsurface resistivity distributions by iteratively minimizing data residuals. The mapping from the subsurface resistivity model to the measured EM fields is typically non-linear and can be expressed as

$$\mathbf{d} = F(\mathbf{m}), \tag{1}$$

where $F$ denotes the forward operator, $\mathbf{d}$ represents the synthetic EM data, and $\mathbf{m}$ describes the geoelectrical properties of the medium. Under the deterministic inversion framework, due to the fact that the high-dimensional model space cannot be uniquely constrained by limited observations, a regularization term based on Tikhonov theory (Tikhonov and Arsenin 1977) is incorporated to construct the objective function, i.e.

$$\Phi(\mathbf{m}) = \mathcal{D}\left\{W_d(\mathbf{d}_{obs}, \mathbf{d}_{pred})\right\} + \lambda \mathcal{R}\left\{(\mathbf{m}, \mathbf{m}_{ref})\right\}, \tag{2}$$

where $\mathcal{D}$ measures the misfit between observed data $\mathbf{d}_{obs}$ and synthetic responses $\mathbf{d}_{pred}$, $W_d$ denotes the data weighting matrix constructed from observational errors, $\mathcal{R}$ denotes the model regularization term, and $\lambda$ is a trade-off parameter that balances the data misfit and regularization term. The data misfit can take various forms, such as L1 norm, L2 norm, Wasserstein distance, or Sinkhorn distance (Yang et al. 2026).

The optimization often adopts a gradient descent strategy by starting from an initial model $\mathbf{m}_0$ and updating the model iteratively until the data misfit satisfies a predefined convergence criterion. For example, at the $k$+1-th iteration, the model parameters are updated by

$$\mathbf{m}_{k+1} = \mathbf{m}_k - \alpha_k \frac{\partial \Phi(\mathbf{m})}{\partial \mathbf{m}_k}, \tag{3}$$

where $\Phi(\mathbf{m})$ is the objective function defined in equation (2), and $\partial\Phi(\mathbf{m})/\partial\mathbf{m}_k$ denotes the sensitivity matrix dictating the descent direction. The gradient is typically computed using the adjoint-state method or automatic differentiation techniques (Sambridge et al. 2007; Liu et al. 2025; Li et al. 2026b), and $\alpha_k$ represents the step size for model update.

### 2.2 MCSEM Inversion via Deep Reparameterization

The concept of deep reparameterization was first introduced in the field of computer vision as an advancement over conventional data-driven paradigms. Traditionally, the application of deep learning to inverse problems relies heavily upon end-to-end pre-training with massive datasets. The Deep Image Prior (DIP) framework introduced by Ulyanov et al. (2018) alters this paradigm, demonstrating that an untrained convolutional neural network architecture can achieve unsupervised image restoration without requiring external training data. This breakthrough reveals that the hierarchical structure and parameterization of deep neural networks act as an implicit regularization mechanism. During the gradient-based optimization, the underlying non-linear dynamics bias the network to preferentially fit low-frequency, continuous physical signals while effectively suppressing high-frequency random noise (Rahaman et al. 2018). Inspired by this intrinsic property, seismologists incorporated the DIP framework into seismic full-waveform inversions by reparametrizing subsurface models through deep generator networks to capture latent geostatistical features (He and Wang 2021; Zhu et al. 2022; Wang et al. 2023; Sun et al. 2023; Liu et al. 2026a). As illustrated in Fig. 1, the generator network maps a fixed-dimensional random input vector $\mathbf{I}_r$ to a resistivity model $\mathbf{m}$ by

$$\mathbf{m} = \psi_\theta(\mathbf{I}_r), \tag{4}$$

where $\theta$ represents the optimizable parameters of the generator network $\psi_\theta(\cdot)$. The random vector $\mathbf{I}_r$ is typically sampled from a standard normal distribution and remains invariant throughout the optimization. Its structural dimensionality depends on the network type, manifesting as a 1D vector in multilayer perceptrons or 1D convolutional networks, or a 2D random field in architectures like U-Net. Regardless of the input form, $\psi_\theta$ ensures that the output dimension matches the targeted resistivity model through upsampling, convolution, and reshaping operations.

Based on the reparameterization, the objective function for MCSEM inversion in equation (2) is reformulated as

$$\Phi(\mathbf{m}) = \mathcal{D}\left\{W_d[\mathbf{d}_{obs}, F(\psi_\theta(\mathbf{I}_r))]\right\} + \left\{\psi_\theta(\mathbf{I}_r)\right\}, \tag{5}$$

which concurrently serves as the loss function for training the generator network, with the ultimate predicted model given by $\mathbf{m}^* = \psi_{\theta^*}(\mathbf{I}_r)$. Note that as the regularization constraints are implicitly embedded within the network architecture, equation (5) eliminates the need for any explicit regularization terms. Through reparameterization, the optimization is transformed from model space $\mathbf{m}$ to parameter space $\theta$. The gradient propagation is derived via the chain rule by integrating the model-space gradient $\partial\Phi(\mathbf{m})/\partial\mathbf{m}$ with the network parameter gradient $\partial\mathbf{m}/\partial\theta$ and can be written as

$$\frac{\partial\Phi(\mathbf{m})}{\partial\theta} = \frac{\partial\Phi(\mathbf{m})}{\partial\mathbf{m}} \cdot \frac{\partial\mathbf{m}}{\partial\theta} = \frac{\partial\Phi(\mathbf{m})}{\partial\psi_\theta(\mathbf{I}_r)} \cdot \frac{\partial\psi_\theta(\mathbf{I}_r)}{\partial\theta}, \tag{6}$$

where $\partial\psi_\theta(\mathbf{I}_r)/\partial\theta$ denotes the neural Jacobian matrix representing the sensitivity of network outputs to parameters $\theta$ that can be efficiently computed via automatic differentiation in frameworks like PyTorch. The term $\partial\Phi(\mathbf{m})/\partial\psi_\theta(\mathbf{I}_r)$ represents the sensitivity of the objective function to model parameters $\mathbf{m}$, acquired through adjoint forward modelling or automatic differentiation. Consequently, the iterative update in parameter space can be written as

$$\theta_{k+1} = \theta_k - \alpha_k \frac{\partial\Phi(\mathbf{m})}{\partial\theta_k}, \tag{7}$$

where $\alpha_k$ is the learning rate of the optimizer at the $k$-th iteration.

The equations presented above establish the theoretical foundation for MCSEM inversion via deep reparameterization. By replacing the conventional sensitivity matrix with the neural Jacobian matrix, this method incorporates implicit prior information and physical non-linearities into the gradient propagation paths. However, due to the severe non-linearity governing EM fields and the complex interactions between deep reparameterization networks and forward solvers, the practical application of this approach remains highly challenging. Furthermore, an effective integration of prior information regarding physical properties

provided by independent geophysical methods is important for accelerating convergence and mitigating the non-uniqueness of the inversions.

### 2.3 Reference-Guided Deep Reparameterization

To effectively leverage the prior information, in the reference-guided DIP strategies the conventional random noise input is replaced by a specified reference model. Zhao et al. (2020) first introduced reference-guided DIP approach, and demonstrated that an initial solution closer to the target model enhances reparameterization performance, though the network still requires random initialization and training from scratch. Consequently, this approach frequently requires thousands of optimization iterations and thus incurs substantial computational costs. In this study, we will evaluate three distinct strategies for integrating reference models into the deep reparameterization framework (Fig. 2).

a) Direct reference model input (Zhao et al. 2020): The reference model $\mathbf{m_0}$ directly replaces the original random vector input of the generator network, and yields the reparameterization subsurface model, i.e.

$$\mathbf{m} = \psi_\theta(\mathbf{m}_0) . \tag{8}$$

b) Perturbation prediction (Zhu et al. 2022): The generator network retains a random vector input but is tasked solely with predicting the perturbation between the true model and the initial reference model. During the inversion, the resistivity model is obtained by superimposing the network output onto the reference model, i.e.

$$\mathbf{m} = \psi_\theta(\mathbf{I}_r) + \mathbf{m}_0 . \tag{9}$$

c) Reference model warm-up training (He and Wang 2021): Prior to the physics-driven inversion, the generator network undergoes pre-training to establish a mapping from the random vector to the reference model. The objective function for this warm-up stage is defined as

$$\theta^* = \arg\min_{\mathbf{m}} \left( \left\| \psi_\theta(\mathbf{I}_r) - \mathbf{m}_0 \right\|_2^2 \right) . \tag{10}$$

Upon the completion of the warm-up stage, the pre-trained network generates the input resistivity model for the subsequent inversions, denoted by $\mathbf{m}^* = \psi_{\theta^*}(\mathbf{I}_r)$, is iteratively updated during the inversion.

### 2.4 Deep Ensemble Strategy for Uncertainty Quantification

Although the single reparameterization neural network can reconstruct the subsurface resistivity model, the resulting point estimate $\theta^*$ cannot characterize the probability distribution of the equivalent solution space. Given that the objective functions in geophysical EM inversions exhibit prominent non-convexity and multi-modal characteristics, a deep ensemble approach is incorporated into the reparameterization framework to quantify the uncertainty induced by physical non-uniqueness. The algorithm initializes an ensemble of $K$ neural networks sharing identical architecture but having distinct, randomly initialized weights, denoted as $\left\{NN_{\theta_k}\right\}_{k=1}^{K}$. Under a fixed random input vector $\mathbf{I}_r$, each network undergoes independent, parallel gradient descent optimization driven by data residuals. Owing to the highly non-convex loss landscape of high-dimensional neural networks, distinct initialization trajectories guide individual networks to converge into mutually independent local optimal regions $\theta_k^*$. Following the optimization, the converged weights of the networks are mapped back into the physical model space, yielding a model ensemble $\left\{\mathbf{m}_k = NN_{\theta_k^*}(\mathbf{I}_r)\right\}_{k=1}^{K}$ that contains $K$ potential solutions. Based on this ensemble, the statistically robust expected resistivity model $\mathbb{E}[\mathbf{m}]$ is obtained through the sample mean, i.e.

$$\mathbb{E}[\mathbf{m}] \approx \bar{\mathbf{m}} = \frac{1}{K}\sum_{k=1}^{K}\mathbf{m}_k , \tag{11}$$

while the posterior model variance $\mathbb{V}[\mathbf{m}]$ is expressed as

$$\mathbb{V}[\mathbf{m}] \approx \sigma_{\mathbf{m}}^2 = \frac{1}{K}\sum_{k=1}^{K}(\mathbf{m}_k - \bar{\mathbf{m}})^2 . \tag{12}$$

Compared to single point estimates, the deep ensemble preserves the implicit smoothing and edge-preserving advantages in deep reparameterization. Furthermore, the calculated

296 variance $\sigma_{\mathrm{m}}^2$ quantitatively maps deep formations or complex structural boundaries where data
297 constraints are weak and provides a rigorous metric for comprehensive interpretation and risk
298 assessment.

299 For the highly ill-posed MCSEM inverse problems, the deep ensembles typically generate
300 equivalent models with diverse structural morphologies, thereby forming complex multi-modal
301 posterior distributions. Directly applying a global arithmetic average for posterior estimation
302 can cause a smoothing effect due to misaligned boundaries among different equivalent models,
303 which will blur genuine physical interfaces and artificially exaggerate the thicknesses of
304 anomalies (Tarantola 2005; Sen and Stoffa 2013). To circumvent this limitation, in the present
305 study we introduce a posterior interpretation scheme based on the joint optimization of
306 unsupervised clustering and global interface probability. This scheme first applies an
307 unsupervised clustering mechanism to partition the equivalent models into geologically distinct
308 subsets, which effectively untangles the spatial aliasing induced by non-uniqueness and
309 prevents the failure of mean-field approximations under multi-modal distributions.
310 Subsequently, the cluster selection is executed by computing the spatial gradients of the
311 ensemble models. When calculating the spatial gradient of the model, we first transform the
312 logarithmic resistivity values into the constant domain and then compute the absolute
313 differences in resistivity between adjacent layers, which are compared against a predefined
314 threshold. Within data residual tolerances, the subset maximizing the inner product with the
315 global interface probability is selected as the representative inversion outcome. If multiple
316 clusters achieve the same final score, the cluster with the lowest overall data misfit is selected.
317 This mechanism retains the structural diversity inherent in the solution space while isolating
318 optimal equivalent models characterized by physical self-consistency and sharp boundaries. Fig.
319 2 illustrates the operational workflow of the developed deep ensemble inversion framework
320 coupled with the joint-selection mechanism. The algorithmic implementation of the developed
321 Swi-DREI methodology is detailed in Algorithm 1.

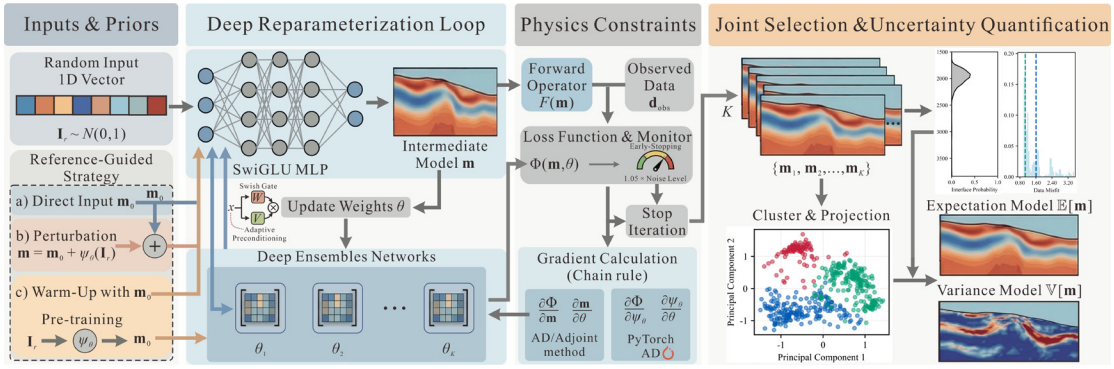



**Figure. 2** Workflow of the physics-driven deep reparameterization ensemble inversion framework for uncertainty quantification. Initially, a 1D random vector or reference model is fed into the generator network to construct the initial ensemble of subsurface resistivity models. Subsequently, each model undergoes forward simulation to obtain data residuals, and the gradients are calculated via the adjoint-state method or automatic differentiation to update parameters of the ensemble networks in parallel (the ensemble scale is set to $K$ = 500 in this study). Once the network ensemble satisfies the convergence criteria, a joint optimization strategy that combines unsupervised clustering and global interface probability is deployed to interpret the final inversion results.

**Algorithm 1** Swi-DREI Optimization and Cluster Selection Framework.

---

**Require:** $\mathbf{d}_{obs}$, $\mathbf{I}_r$, $\mathbf{m}_0$, $K$, $N$iters

1: Initialize $K$ independent, untrained networks $\left\{NN_{\theta_k}\right\}_{k=1}^{K}$

2: **for** i = 1,…, $N$iters **and** $\mathbf{d}_{residual}$ > tolerance **do**

3: **for** k = 1,…, $K$ **do**

4: $\mathbf{m}_k = NN_{\theta_k^*}(\mathbf{I}_r)$

5: $\Phi(\mathbf{m}_k) = \mathcal{D}\left\{W_d[\mathbf{d}_{obs}, F(NN_{\theta_k^*}(\mathbf{I}_r))]\right\} + \left\{NN_{\theta_k^*}(\mathbf{I}_r)\right\}$

6: $\mathbf{g} = \partial\Phi(\mathbf{m})/\partial\theta_k$

7: $\theta_k^{(i+1)} = \mathrm{Adam}(\theta_k^{(i)}, \mathbf{g}\theta)$

8: **end for**

9: **end for**

10: Global interface $P_{\mathrm{interface}} = count(\nabla m_k > \mathrm{threshold})/K$

11: K-means Cluster and maximizing the inner product with global interface $\langle \nabla m_{\mathrm{cluster}}, P_{\mathrm{interface}} \rangle$

12: Calculate the global and cluster mean and variance

## 3. Numerical Experiments

### 3.1 Benchmark Model

To verify the effectiveness of the deep ensemble reparameterization inversion framework, we first conduct numerical experiments using the classic thin-layer model of hydrocarbon reservoir (Key 2009). All numerical computations are performed on an NVIDIA RTX 4090 GPU within the PyTorch framework. To achieve efficient adaptation with neural network reparameterization, we introduce a pre-trained forward operator (Liang et al. 2024) to replace conventional numerical modeling solvers. This approach improves computational efficiency while using automatic differentiation to compute exact gradients during the backpropagation. Table 1 summarizes the key parameters governing the forward modeling and inversion. Specifically, the simulated marine environment features a seawater depth of 1500 m and a resistivity of 0.3 Ω·m. The survey configuration consists of a horizontal electric dipole transmitter located at a depth of 1450 m with a transmitting current of 1 A and a dipole length of 200 m, the seafloor receivers are positioned at a depth of 1500 m. We calculate the inline x-electric field for frequencies ranging from 0.2 Hz to 2.9Hz and offsets ranging from -10,000 to 10,000 m (*see* Table 1).

**Table 1** Key parameters for our forward and inverse simulations.

| System Configuration | Simulation Parameters |
|---|---|
| Seawater depth: 1500m | Data type: Amplitude and phase |

| | |
|---|---|
| Seawater resistivity: 0.3 Ohm-m | Component: Inline *x*-electric field |
| Dipole length: 200m | 0.2 Hz: [−10,000, 10,000] m |
| Transmitting current: 1A | 1.2 Hz: [−6,000, 6,000] m |
| Transmitter location: 1450m | 2.0 Hz: [−5,000, 5,000] m |
| Receiver location: 1500m | 2.9 Hz: [−4,000, 4,000] m |

The network employs the Adam optimizer (Kingma and Ba 2014) with an initial learning rate of $10^{-4}$ that is decayed by a factor of 0.8 every 200 iterations up to a maximum of 1000 iterations. For the warm-up training, the network is required to first resolve the mapping from random vectors to the initial model, utilizing a learning rate of $5\times10^{-4}$ for 500 iterations. The loss function for the reparameterization inversion is defined as L2 norm of the discrepancy between the observed and predicted data. To mitigate the risk of overfitting, an early stopping criterion is incorporated to monitor the optimization process. For synthetic data, a threshold is set at 1.05 times the root-mean-square (RMS) error between the noise-free and noise-contaminated data. The optimization process automatically terminates and the final inverted models are yielded once the mean error of the ensemble reaches this predefined threshold. This is to ensure that the network extracts valid physical signals from the measured data. The network architecture and hyperparameter settings can be found in Appendix A.

## 3.2 Synthetic Tests

### 3.2.1 1D Reservoir Models

We first designed a classic 1D thin reservoir model commonly utilized in MCSEM exploration, designated as Model 1. As illustrated in Fig. 3, this model exhibits a three-layer structure comprising of an overlying sedimentary layer, a thin reservoir, and an underlying sedimentary layer. We add 5% Gaussian random noise to the synthetic EM responses to construct the inversion data. During the inversion process, we set the initial subsurface resistivity to 1 Ω·m and the total number of model layers to 30. The thickness of the first layer is 25 m, and the thicknesses of subsequent layers increase by a factor of 1.1, terminating with a uniform half-space. Previous studies indicate that the mainstream strategies for deep reparameterization inversion primarily include perturbation prediction defined in equation (9) and warm-up

training formulated in equation (10). Thus, here we exclusively present the inversion results of these two strategies. In this model test, the Swi-DREI under both strategies executes 1000 iterations, with an average computational time of 135.36 s. Fig. 3 shows the inversion results and data misfits. As observed from Figs. 3a and 3e, the model ensembles generated by both strategies demonstrate high consistency in resistivity distribution. The narrow distribution range in the shallow region reflects strong constraints from the data, indicating high reliability of the inversion results. The distributions of the high-resistivity target and its adjacent layers broaden significantly, reflecting the non-uniqueness of MCSEM inverse problems. The posterior resistivity distributions and histograms indicate that although several individual models underestimate the resistivity of the target layer, they exhibit high probability density near the true value. Combining the electrical interface probabilities in Figs. 3b and 3f, we can accurately determine the resistivity and spatial localization of the target layer. As the depth increases, the EM fields undergo severe attenuation induced by both the overlying formations and high-resistivity thin layer, which causes the distribution range within deep sedimentary formations to expand further and the uncertainty to increase correspondingly. In addition, the data misfits in Figs. 3d and 3h reveal that both strategies converge effectively, with RMS values mainly concentrated around 1.6, validating the reliability of the inversion results. A comprehensive comparison reveals that the perturbation prediction strategy outperforms the warm-up training strategy in terms of the recovery of deep formations.

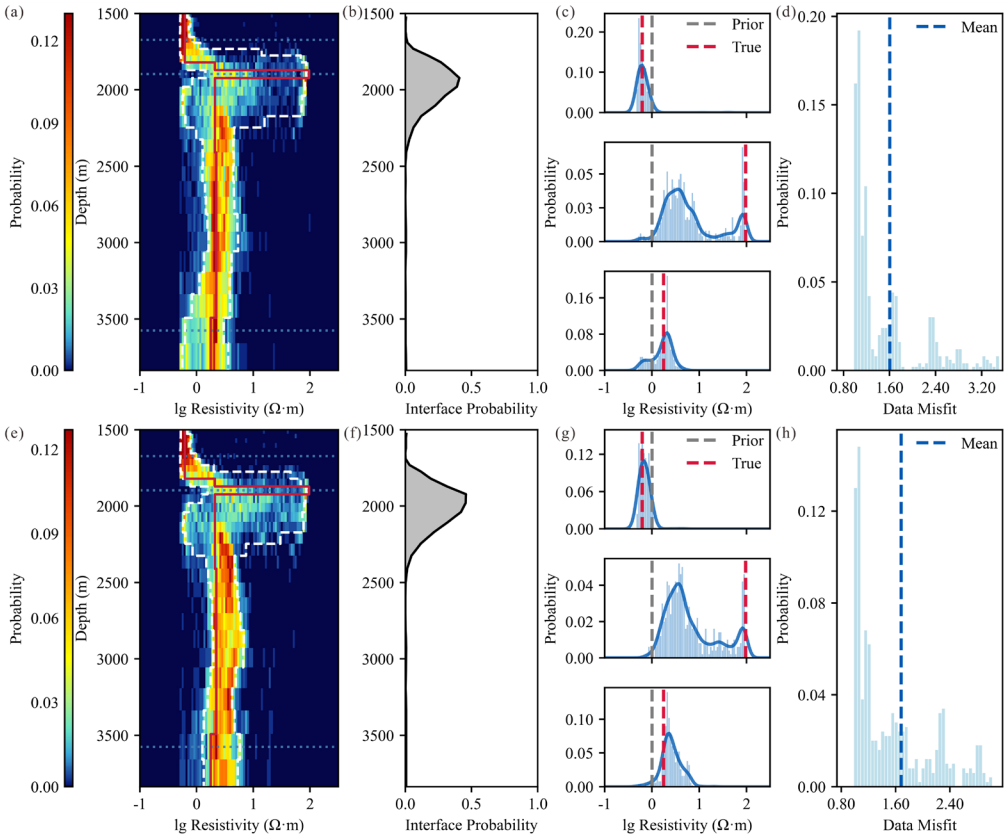



**Figure. 3** Inversion results of the thin reservoir model (Model 1). Subplots (a)-(d) display the inversion results of the perturbation strategy, while (e)-(h) display the results of the warm-up strategy. Subplots (a) and (e) illustrate the posterior distributions of the resistivity models obtained via the Swi-DREI framework. The red solid lines represent the true resistivity model, whereas the white dashed lines mark the 5% to 95% distribution interval. The blue dashed lines indicate the horizons displayed in the resistivity histograms in subplots (c) and (g). Subplots (b) and (f) are the geoelectrical interface probability acquired by conducting statistical analysis on the inter-layer resistivity differences across 500 posterior models. Subplots (c) and (g) display the posterior resistivity distribution histograms for the specified horizons in subplot (a) and (e), where the red dashed line represents the true resistivity, the gray dashed lines represent the prior resistivity values, and the blue solid lines represent the smooth estimation curve representing the posterior probability density. Subplots (d) and (h) show the data misfit ( Data misfit $= \sqrt{1/N_d\,(\mathbf{d}_{obs}-\mathbf{d}_{pred})^T W_d^T W_d\,(\mathbf{d}_{obs}-\mathbf{d}_{pred})}$ ), with the blue dashed line illustrating the average data misfit.

In the following, we further test a reservoir model with a larger burial depth, designated as Model 2. In this model, the top interface of the reservoir is located approximately 800 m below the seafloor. The basement has a resistivity slightly higher than the overlying sedimentary layer and is located at a depth of 3500 m. For this model, the initial model is assumed to be a uniform half-space of 3 Ω·m. Both inversion strategies reach the maximum number of iterations. Figs. 4a and 4e present the posterior distributions of the inversion results. As illustrated in these subplots, due to the higher resistivity of the shallow sedimentary layers, the corresponding resistivity distribution is broader than that of Model 1, but most of the inverted models still concentrate near the true value. In contrast, the resistivity distribution near the target layer diverges significantly, and most predicted values are biased low. This phenomenon primarily attributes to the reduced sensitivity of EM signals to deeply buried high-resistivity targets, which further limits the capability of the inversion algorithm to delineate the layer resistivity. Nevertheless, the posterior resistivity distribution still exhibits a high probability density near the true value, and the interface probabilities in Figs. 4b and 4f exhibit prominent peaks at the reservoir location. With increasing depth, the uncertainty of the deep high-resistivity basement elevates further. This aligns with the physical characteristics of EM field attenuation with depth, where the constraint of the observed data on the model space weakens, resulting in an expanded resistivity distribution.

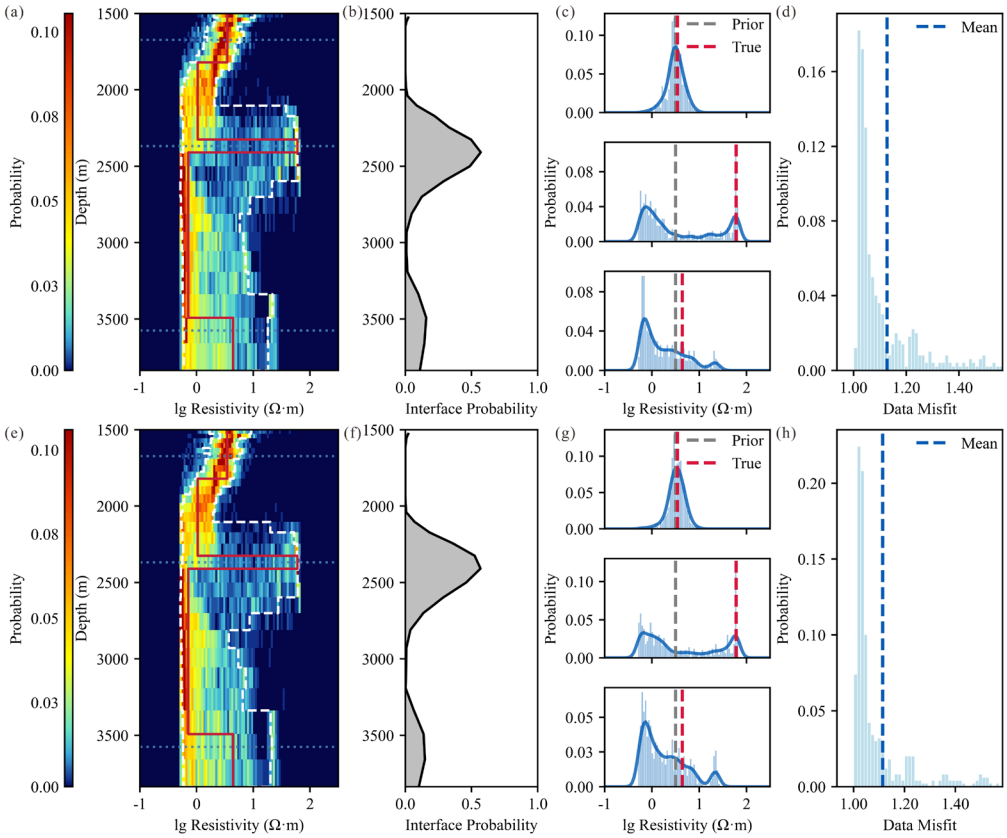



**Figure. 4** Inversion results and data misfits of Model 2. Plots (a)-(d) show the inversion results of the perturbation prediction strategy, while (e)-(h) show the results of the warm-up training strategy.

From above discussions, we see that the two Swi-DREI inversion strategies can both obtain reasonable subsurface electrical distributions. However, the primary exploration targets in MCSEM surveys are typically thin high-resistivity bodies, such as hydrocarbon reservoirs or gas hydrate zones, embedded within low-resistivity sedimentary formations. The identification and resource assessment of such high-resistivity targets rely heavily on the inversion algorithm to accurately delineate geoelectrical interfaces. Since the posterior mean model possesses a smoothing effect, the inversion results frequently exhibit equivalence effect, which blur a high-resistivity thin layer into an equivalent structural unit characterized by lower resistivity and greater thickness. This will make it difficult to do the subsequent geological interpretation. Thus, in this study we adopt an unsupervised clustering method to partition the model ensemble and combine interface probability to optimize the mean model of each category, with the aim to extract the model subset that is physically self-consistent and closest to the true model.

For the two numerical examples in the above sections, we employ the K-Means clustering method. Numerical experiments indicate that the optimal number of clusters is 5 (refer to supplementary materials Fig. S1-S4 for the experimental basis of cluster selection), and the clustered inversion results are illustrated in Fig. 5. It is seen from the figures that influenced by the global smoothing effect, the global mean models exhibit obvious over-smoothing phenomena at the target region, struggling to accurately present resistivity values and spatial location. In contrast, the clustered mean models effectively mitigate this limitation. Through the joint screening of data misfit and interface probabilities, an optimal cluster that balances the data fitting and interface characterization is isolated from the posterior model ensemble. This process requires no additional prior information, provides a reference for field data inversion and geological interpretation. Additionally, to visually demonstrate the partitioning of the high-dimensional model space, the final clustered models are projected onto a 2D plane via principal component analysis (PCA), retaining exactly the first two principal components for plotting. The resulting PCA dimensionality-reduced scatter plots within the model space reveal that the clustering performance for Model 1 is inferior to that for Model 2, with the distribution of the optimal cluster for Model 1 being relatively dispersed. Combining the data fitting curves in supplementary materials Figs. S5-S8 and the cluster analysis in Fig. S9, it becomes evident that the posterior model ensemble of Model 1 contains several individual models with poor data fitting, and the number of models in the optimal cluster is relatively small. Conversely, Model 2 exhibits a higher consistency in data fitting, the corresponding optimal cluster comprises a larger number of models, and the associated distribution demonstrates a higher degree of concentration.

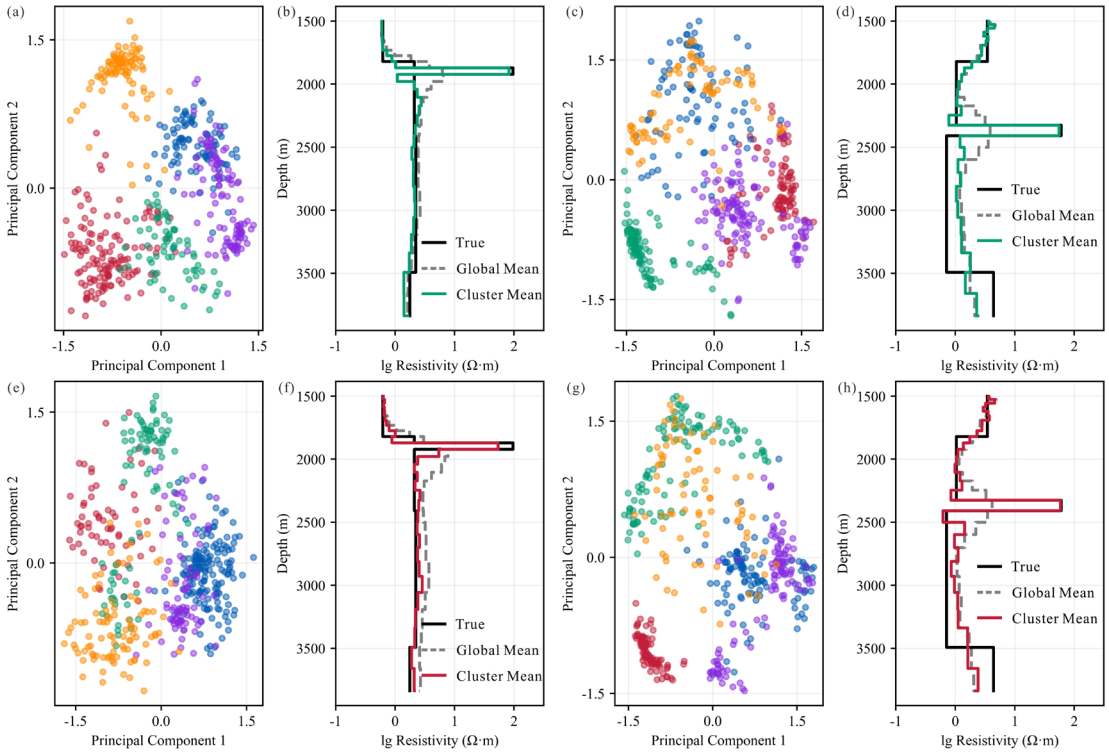



**Figure. 5** PCA dimensionality-reduced scatter plots of the model space based on K-Means clustering and the corresponding clustered mean models. Subplots (a)-(d) show results for the perturbation strategy of Model 1 and Model 2, respectively. Subplots (e)-(h) present the results for the warm-up strategy of Model 1 and Model 2. The colors of the respective mean curves in the inversion profiles are consistent with the colors of the corresponding clusters in the left scatter plots.

### 3.2.2 2D Salt Dome Model

To further evaluate the performance of our Swi-DREI algorithm, we construct a 2D salt dome model as shown in Fig. 6. The model consists of conductive sedimentary formations, a high-resistivity thick salt body, a high-resistivity thin reservoir, and an undulating high-resistivity basement. The survey parameters for this model remain consistent with the aforementioned 1D case. The survey line has a total length of 4 km, with 81 measurement stations deployed.

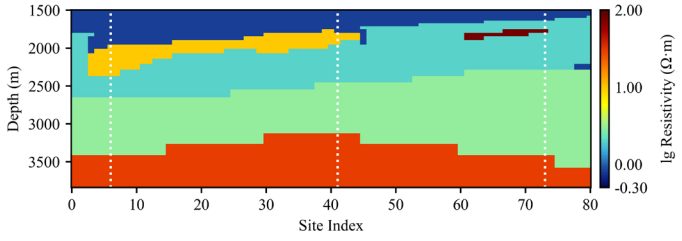


**Figure. 6** A 2D salt dome model (modified from Key, 2016). The white dashed lines indicate the locations of the 1D profiles shown in subsequent sections.

To invert the 2D salt dome model in Fig. 6, we select as the initial model a uniform half-space of 3 $\Omega \cdot$ m. Fig. 7 shows the Swi-DREI inversion results. As observed from the global mean models provided in Figs. 7a and 7b, the results of both inversion strategies exhibit high consistency, which accurately reconstruct the fundamental subsurface geoelectrical structures. Comparatively, the reconstruction quality regarding the resistivity magnitude and geometry of the salt dome achieved by the Swi-DREI scheme outperforms that of the thin-layer reservoir. Affected by the reservoir of high resistivity and small thickness, the global mean results exhibit an obvious smoothing effect, merely reflecting the approximate location and electrical property of the anomaly. In contrast, the clustered mean models in Figs. 7c and 7d recover the spatial localization and resistivity magnitude of the reservoir more accurately: the inverted structures for the salt dome are thinner and possess higher resistivity than those of the global mean models. It is evident that the clustered results are better suited for identifying the anomalous high-resistivity thin layer. Furthermore, the inversion results of the perturbation strategy recover the resistivity and shape of the salt dome and reservoir better than the warm-up strategy. The corresponding standard deviation and interface probability distributions clearly delineate the two high-resistivity anomalous zones, with the uncertainty near the thin reservoir being significantly larger than those in the surrounding areas. Although the resistivity inversion results fail to fully reconstruct the true depth of the high-resistivity basement, from Figs. 7e and 7f we can see that the standard deviation increases significantly at the true basement depth, which effectively indicates the location of the electrical interface and verifies the validity of the uncertainty assessment within the proposed framework.

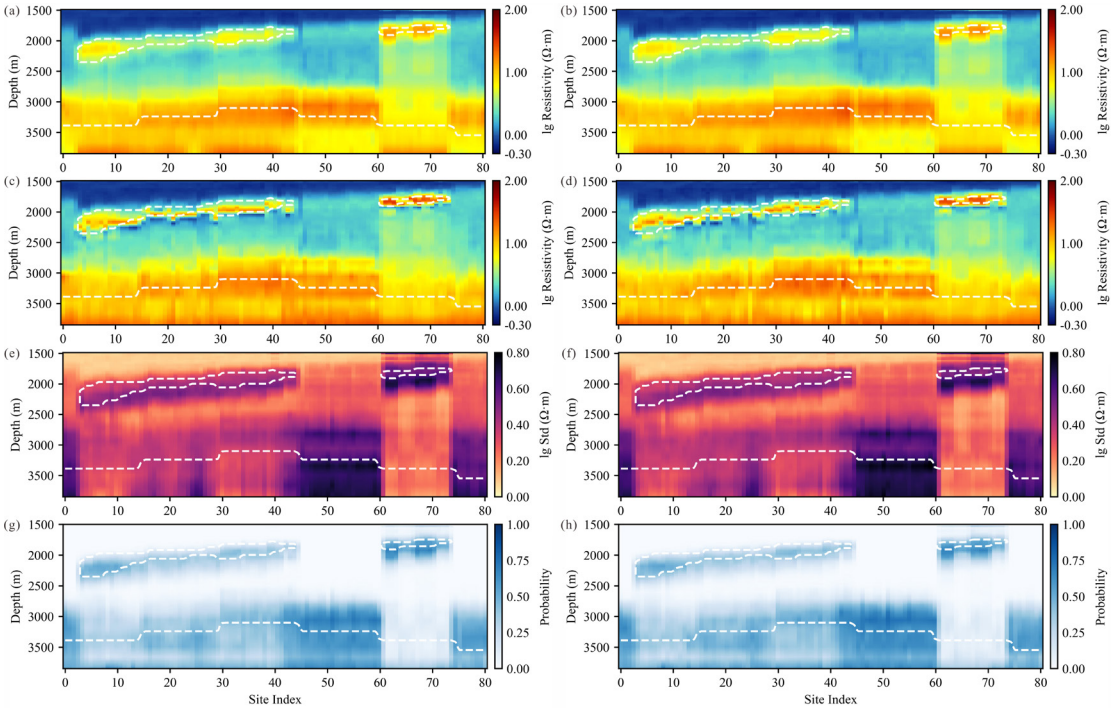



**Figure. 7** Inversion results of the 2D salt dome model. Panels (a), (c), (e), and (g) present the global mean model, clustered mean model, global logarithmic standard deviation, and interface probability profile for the perturbation strategy, respectively, while (b), (d), (f), and (h) present the corresponding results for the warm-up strategy. The white dashed lines demonstrate the contours of the two anomalies and the high-resistivity basement.

Fig. 8 shows the posterior resistivity distributions at three representative stations (marked by white dashed lines in Fig. 6). Given the high similarity in the posterior distributions of both strategies, we only present the results of the perturbation strategy here. The three stations correspond to geological environments characterized by a thick moderate-resistivity layer, an intermediate-thickness moderate-resistivity layer, and a thin high-resistivity layer, respectively. In the shallow sedimentary layers, the ensemble models are tightly distributed near the true values, whereas the posterior resistivity distributions at the high-resistivity horizons diverge significantly. Comparing the results of the first two stations, we find that as the thickness of the high-resistivity layer increases, the capability of the ensemble to resolve the true value improves. The histograms in Figs. 8c and 8g intuitively reflect this trend. With increasing depth, the attenuation of EM fields leads to weakened constraints of the field data on the deep basement, resulting in increased uncertainty. However, most inverted models still approach the true value.

Since the contrast of physical properties at Station 3 is pronounced, the distribution range of the posterior resistivity within the target layer is significantly wider than those observed at the first two stations. As shown in Fig. 8k, although most models distribute between the prior and true values, some models do successfully converge to the true value with high probability density.

In summary, we conclude that the posterior distributions provided by the Swi-DREI framework possess physical validity and high credibility. Fig. 9 presents the clustering analysis results of the model ensemble. As shown by the dimensionality-reduced projection plots, the selected clusters exhibit favorable grouping features with a balanced distribution of cluster members. The inverted profiles confirm that for high-resistivity, thin-layer targets, the clustered mean model holds significant advantages in the parameter characterization. This aligns with the aforementioned conclusions and further validates the effectiveness of the unsupervised clustering strategy in handling complex non-uniqueness cases.

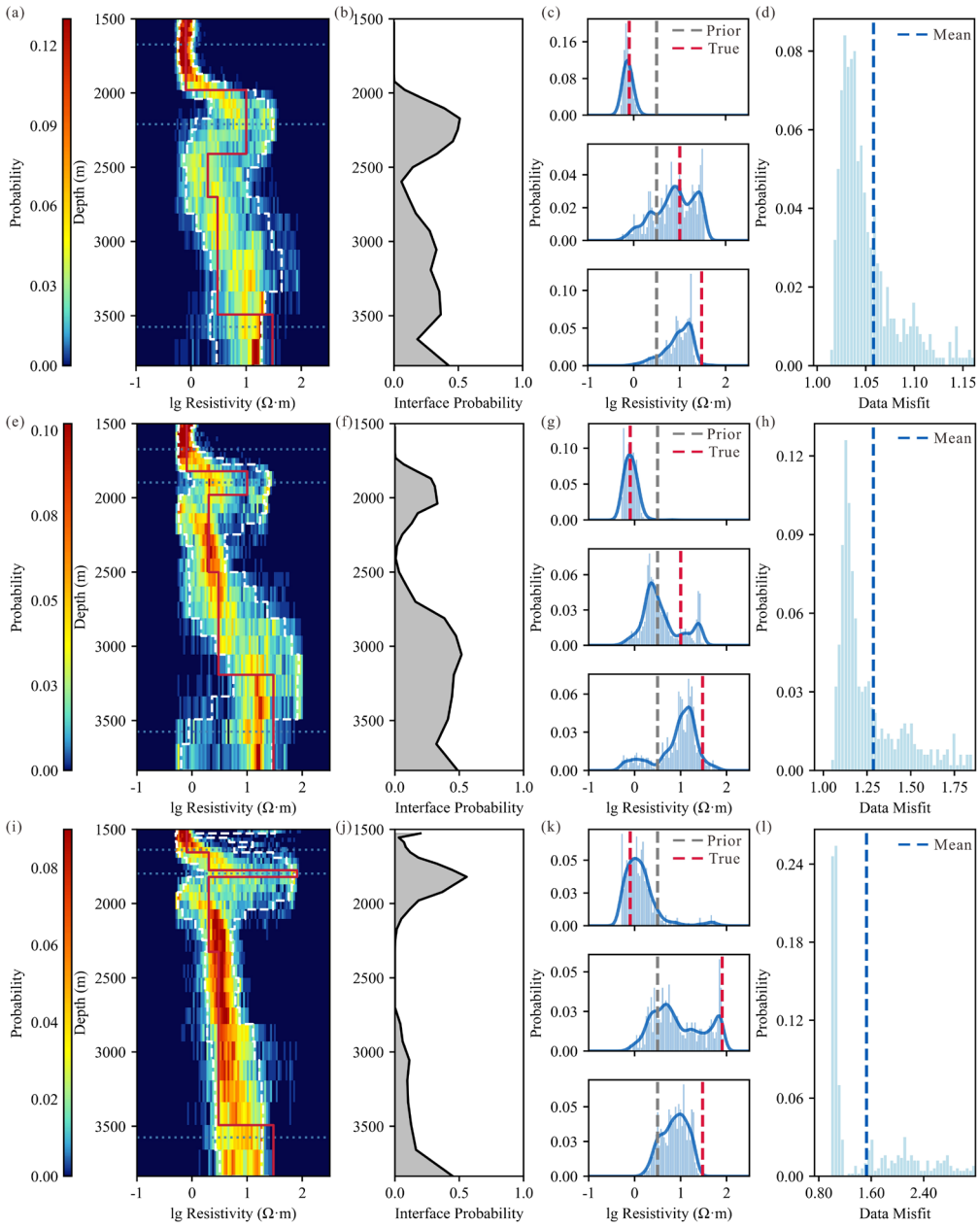



**Figure. 8** Inversion results of the perturbation strategy at stations correspond to the three white dashed lines in the salt dome model of Fig. 6.

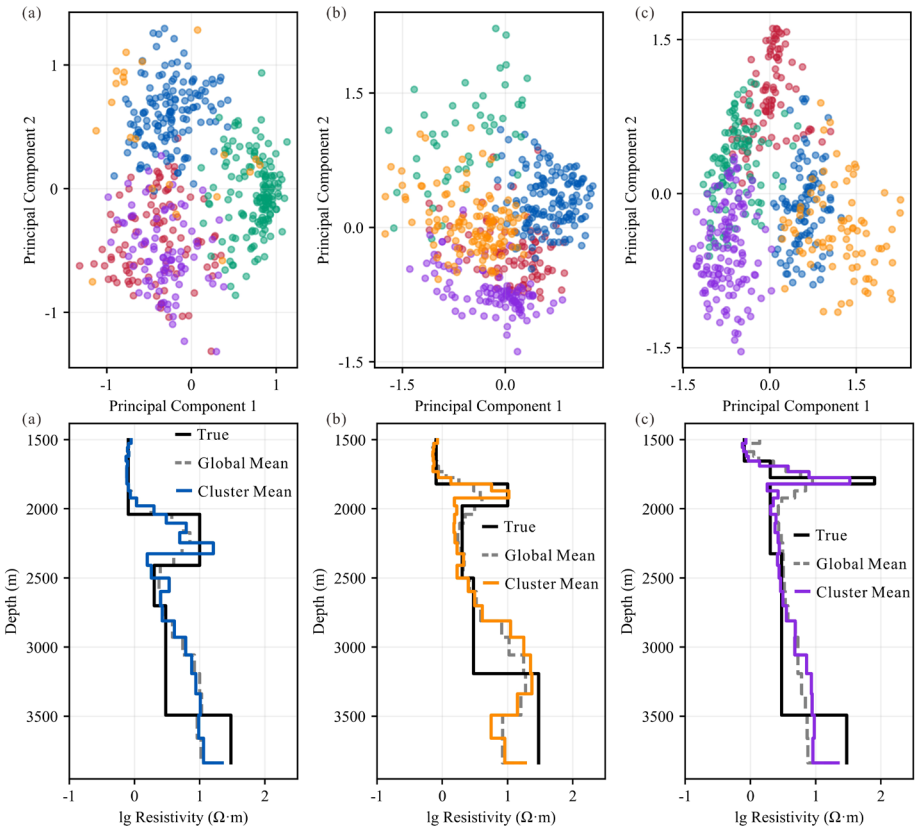



**Figure. 9** PCA dimensionality-reduced scatter plots of the model space after K-Means clustering for the three stations in Fig.7 and the corresponding clustered mean models. In the inversion profiles, the color of the mean curves corresponds to the color of the clusters in the above scatter plots.

### 3.2.3 Robustness Tests

In complex seafloor environment, the measured data inevitably contains noise, making the robustness of inversion algorithms a critical factor for evaluating the exploration accuracy. The conventional gradient-based methods are sensitive to data quality and initial models, often producing biased results and as a result misleading subsequent geological interpretation when processing noise-contaminated data. In this section, we take the 2D salt dome model as an example and assess the robustness of the algorithm under different levels of 1%, 5%, 10%, and 20% Gaussian random noise to the synthetic data. To guarantee statistical randomness, each measurement station employs an independent random seed, thereby decoupling the initialization of the networks from the input datasets. Fig. 10 shows the inversion results of the perturbation strategy under varying noise levels (refer to supplementary materials Fig. S10 for

the warm-up strategy results). As illustrated by the clustered mean models, the reconstruction quality of both anomalous bodies declines as the noise level increases, the tailing artifacts induced by noise get more pronounced within the thin-layer reservoir. In contrast, the global mean models displayed on the right panel exhibit superior resistance to random noise. The geometric morphologies of the anomalies remain stable, with only minor reductions in resistivity magnitudes as the noise gets intensified. This reflects the robustness of the ensemble-based inversion. Since the optimization trajectories of individual models are mutually independent, the global averaging process functions as a statistical filter that suppresses interference from extreme outliers, yielding stable inversion solutions. However, this statistical averaging inevitably leads to degraded spatial resolution and causes over-smoothing artifacts in the generated profiles. Therefore, the clustered mean strategy is required to optimize inversion results that balance high resolution with physical property fidelity. Fig. 11 presents the inverted profiles with the best data fitting at each station. Since the deep reparameterization framework does not introduce explicit spatial regularization constraints, the single individual model profiles exhibit discreteness, characterized by discontinuity in the basement and local oscillations. When the noise level remains below 10%, the reconstruction accuracy of the best-fitting model for the reservoir is comparable to that of the clustered mean, and both outperform the global mean model. As the noise level further increases, the lateral continuity of the inversion results gets weakened significantly, and voids emerge within the anomalies. A joint analysis of these three inverted models facilitates the determination of more accurate and reliable geoelectrical models. Furthermore, as shown in Figure 12, the logarithmic standard deviation increases as the noise ratio increases; the salt dome anomaly indicated by the arrow clearly demonstrates this elevation in uncertainty.

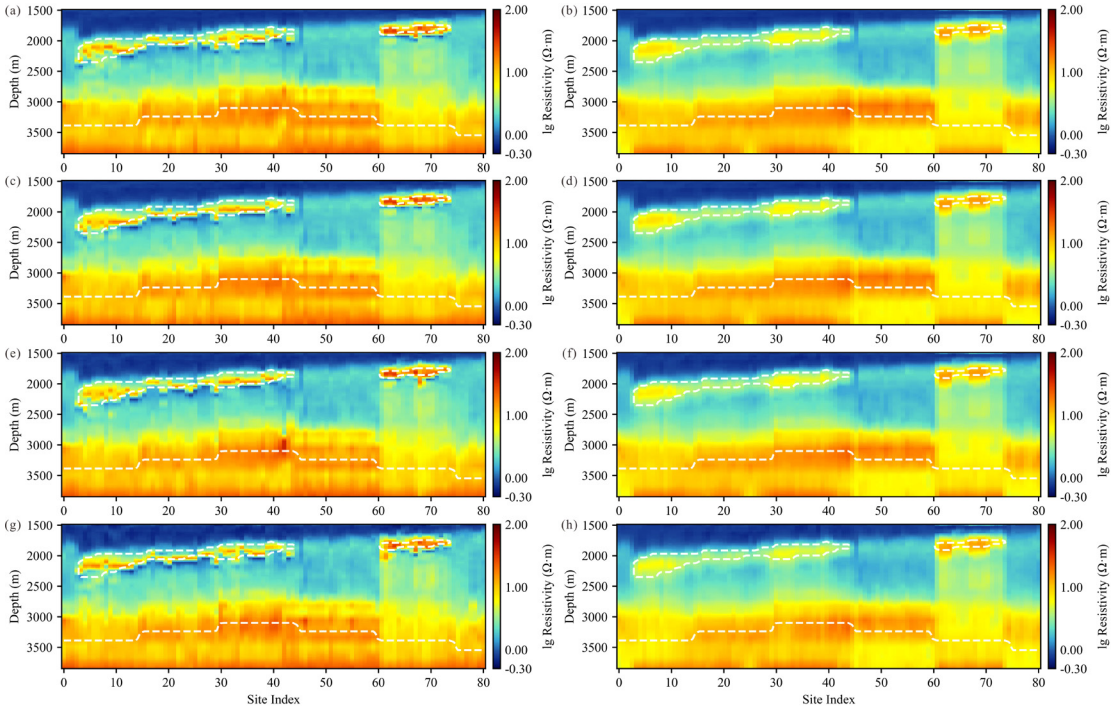



**Figure. 10** Inversion results of the salt dome model with varying noise ratios using the perturbation strategy. From top to bottom, the inversion results correspond to noise levels of 1%, 5%, 10%, and 20%, respectively. The left column shows the clustered mean results, while the right column shows the global mean results.

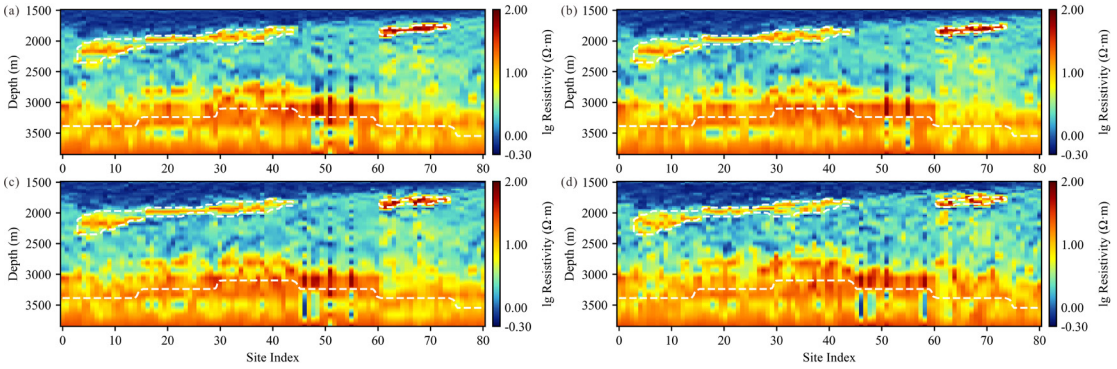



**Figure. 11** Best-fitting models within the ensemble for the perturbation strategy. Plots (a), (b), (c), and (d) correspond to noise ratios of 1%, 5%, 10%, and 20%, respectively.

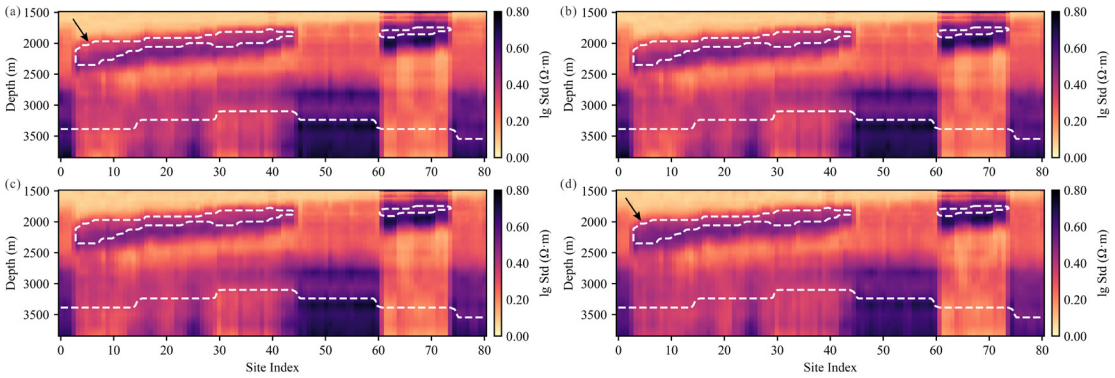



**Figure. 12** Global logarithmic standard deviation of the salt dome model with varying noise ratios using the perturbation strategy. Subplots (a)-(d) correspond to noise levels of 1%, 5%, 10%, and 20%, respectively.

In practical marine EM exploration, the high-density, full-coverage observations in the survey area are often unattainable due to the high costs of seafloor node deployment and recovery, rugged seafloor topography, and ocean currents. The measured EM data frequently exhibit irregular absences in spatial distribution and frequencies. Such data missing significantly exacerbates the ill-posedness of the inverse problem, expanding the null space of the objective function. To verify the practicality of the proposed inversion framework, we test the performance of our Swi-DREI under conditions of random data missing for the salt dome model at a rate of 15%, 35%, and 45% for each station, respectively. A masking technique is adopted during the inversion to process the measured data. The full response is calculated at the forward modelling stage of the predicted model, whereas only unmasked data are preserved during residual calculation and gradient backpropagation. Specifically, the random masking is carried at the individual measurement-point level, where both the amplitude and phase observations at each randomly selected point are simultaneously excluded from the inversion.

Fig. 13 shows the test results. As is observed from the clustered mean results, the lateral continuity of the salt dome and high-resistivity basement get weakened with the increase of the data missing ratio, and the inverted profiles exhibit local oscillations. Simultaneously, the capability of delineating thin reservoir boundaries declines, and the accuracy of the predicted resistivities decreases accordingly. Nevertheless, the overall quality of inversions is less affected by missing data. The global mean results exhibit extreme robustness, with

reconstructions remaining largely unaffected by data missing and showing only slight fluctuations near the high-resistivity basement. However, for the boundary characterization and physical properties of the salt domes and thin reservoirs, the global mean models remain inferior to clustered mean ones. This further supports the conclusion that the global mean models have advantages in inversion stability, whereas the clustered mean models perform better in identifying thin-layer targets and characterizing fine-scale structures. The logarithmic standard deviation illustrated in Fig. 14 demonstrates a monotonic increase relative to the ratio of missing data. This variation is primarily driven by the reduction of observation data constraints, which elevates the uncertainty in the outcomes of the inversion and consequently expands the statistical dispersion of the posterior ensemble.

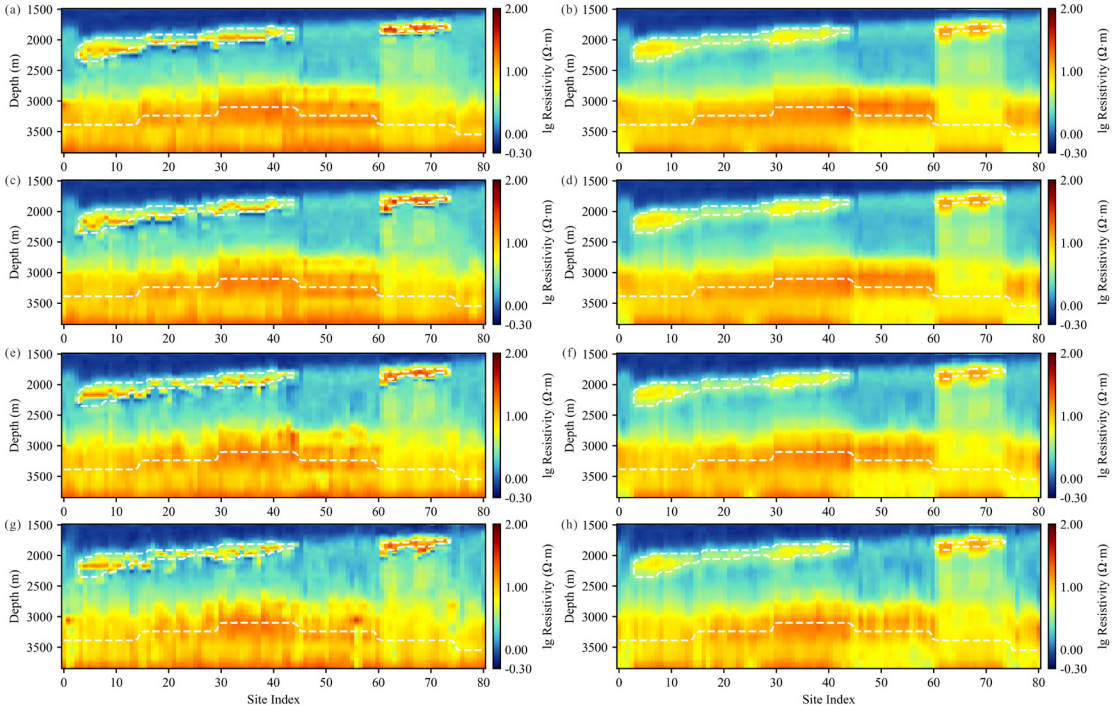



**Figure. 13** Inversion results of the 2D salt dome model with different data missing ratios using the perturbation strategy. The four rows from top to bottom correspond to data missing ratios of 0%, 15%, 35%, and 45%, respectively. The left side shows the clustered mean results, while the right side shows the global mean results.

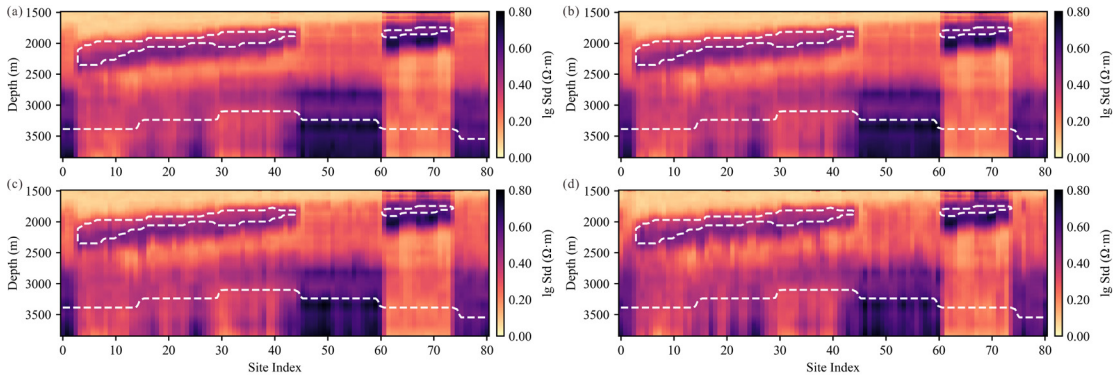



**Figure. 14** Global logarithmic standard deviation of the 2D salt dome model with different data missing ratios using the perturbation strategy. Subplots (a)-(d) correspond to data missing ratios of 0%, 15%, 35%, and 45%, respectively.

## 4. Field Data Application

To validate the effectiveness of the Swi-DREI inversion, we inverted a field survey dataset. The survey features are similar to the synthetic case. Geological data indicate that the basin sequence thickens toward the northeast and thins toward the southwest, showing no evidence of large-scale faulting. The subsurface structure features a high-resistivity basement composed of carbonates and deep-sea fan sandstones. This basement is overlain by a thick sedimentary succession characterized by an alternation of low-resistivity marine mudstones and relatively high-resistivity deep-sea fan sandstone layers, which constitute the primary resistive target zones in the study area.

We perform inversions of 89 stations selected from this area, with system parameters given in Table 1. To evaluate the performance of the Swi-DREI inversion, we compare our results with those obtained from the Occam's inversion and physics-driven deep learning inversion (PhyDnn). The initial model for Swi-DREI is set based on the results from PhyDnn after Gaussian smoothing, the maximum number of iterations is set to 100. The initial model for the Occam's inversion is assumed to be a uniform half-space of 1 Ω·m, the maximum number of iterations is set to 200. Regarding the computational efficiency, the average processing time per station is approximately 84 s for Swi-DREI, compared to roughly 6 min for the Occam's inversion. All profiles exhibit high consistency, with the resistivity structures aligning closely with existing geological data. For brevity, only the inverted profile for survey line 1 is presented

in Fig. 15, whereas the remaining profiles are provided in the Appendix B (Figs. B1-B4). Due to the smoothness constraint, Occam's inversion displays spurious low-resistivity zones at the margins of high-resistivity targets and exhibits poor basement continuity. In contrast, the inverted profiles from PhyDnn and Swi-DREI demonstrate smoother electrical transitions although neither of them incorporates explicit regularization. However, as for the basement characterization, the PhyDnn results appear overly flat, diverging from those of the Occam's inversion and Swi-DREI. Furthermore, the clustered mean model of Swi-DREI preserves more structural details than the PhyDnn and global mean models. The high-resistivity anomalies and electrical interfaces are clearly identified from profiles of logarithmic standard deviation and global interface probability.

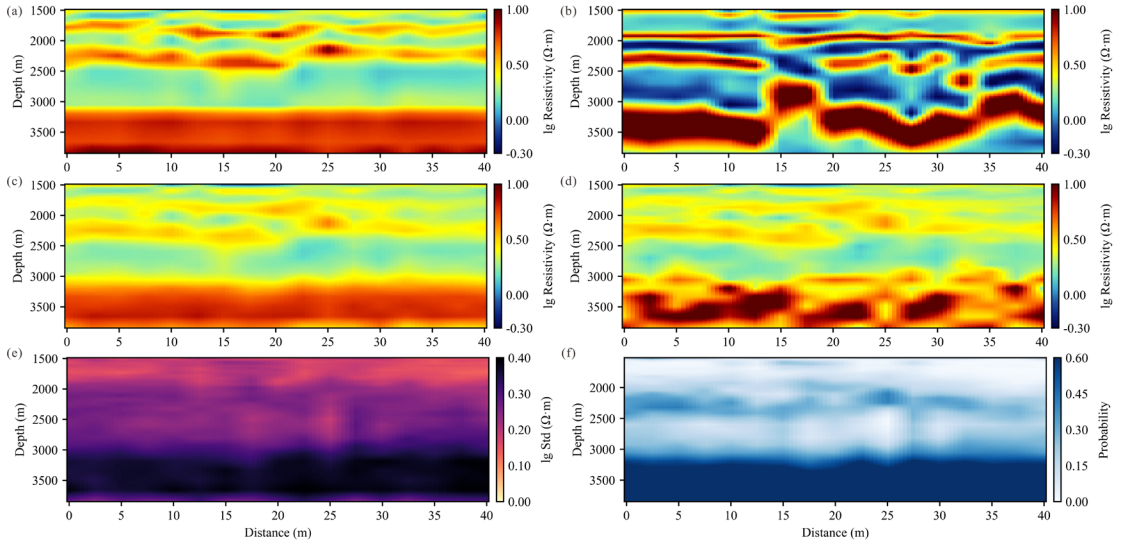
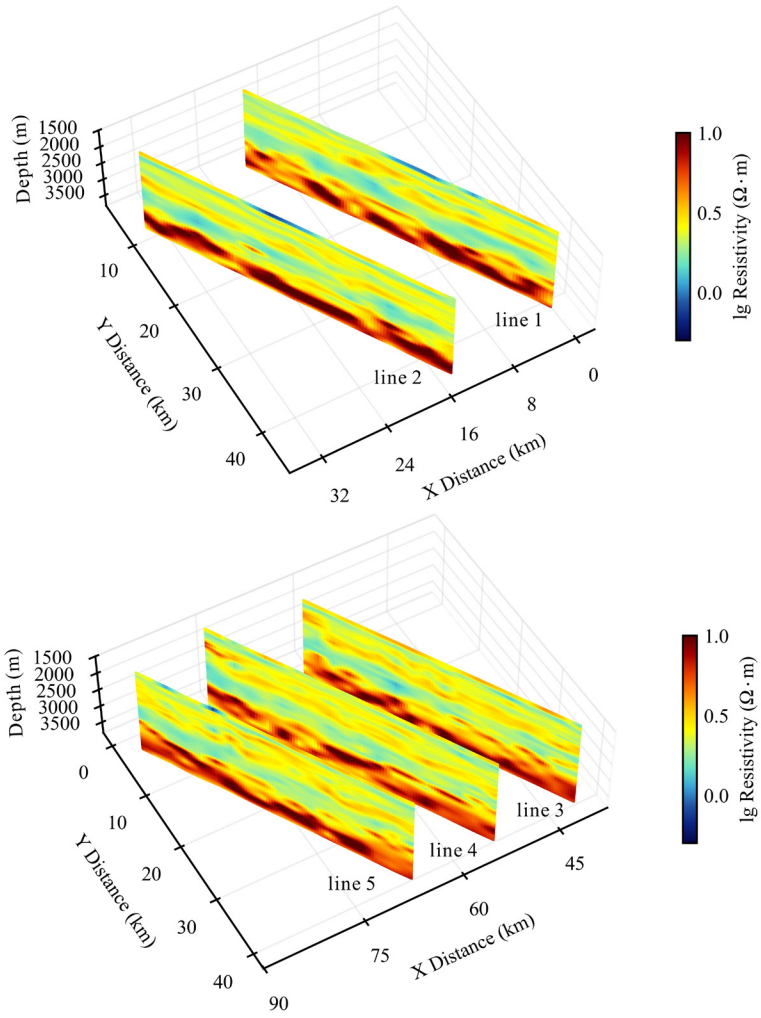



**Figure. 15** Inversion results for Survey Line 1 using the perturbation strategy. (a) Physics-driven deep learning inversion; (b) Occam's inversion; (c) Swi-DREI global mean model; (d) Swi-DREI clustered mean model; (e) global logarithmic standard deviation; (f) global interface probability.

To visually demonstrate the subsurface electrical structure, we construct a quasi-3D profile of the survey area (Fig. 16). The layering reconstructed from the inversion results exhibits a high agreement with the geological sequence. In the deep section of the profile (below 3000 m), a continuous, high-resistivity basement is prevalent across the area. This clearly delineates the spatial distribution of late Cretaceous carbonates and deep-sea fan sandstones which reflects

the basement relief characterized by large depth in the northeast and lower depth in the southwest, which is fully consistent with the northeast-thick and southwest-thin distribution observed in geological records. Above the basement, the inverted profile successfully captures multiple sedimentary sequences with alternating low-high-low resistivity. The layer overlying the basement generally exhibits a significant low-resistivity signature, corresponding to Paleocene to Eocene deep-sea mudstones. Within this low-resistivity background, a strip-like anomaly with weak high-resistivity features is laterally visible, which corresponds to the Eocene deep-sea fan sandstones. Furthermore, the middle section of the profile shifts to a low-resistivity zone, which is consistent with Oligocene to Miocene hemi-pelagic to deep-sea marine mudstones. In the shallower Late Miocene to Pliocene strata, the inversion results clearly reconstruct a high-resistivity feature extending laterally over a significant distance, providing strong evidence for the high-sandstone content and sufficient deep-sea fan deposition during this period. At the uppermost Quaternary level, the inversion profile reverts to a stable low-resistivity signature, controlled by deltaic and shallow marine deposition. Overall, the patterns of resistivity distribution presented in the quasi-3D inversion profile not only reproduce the changes of sedimentary environment of the basin from the Late Cretaceous basement to the Cenozoic, the consistency between the inverted profile and geological data also demonstrates that our Swi-DREI method has the capability to reconstruct subsurface structures in field scenarios.




681

682 **Figure. 16** 3D display of profiles inverted by the clustered mean models using the perturbation
683 strategy. To facilitate a clear visualization of the seafloor structure, an offset of 10 km is applied
684 between survey lines (in *x*-direction) for plotting.

685 Fig. 17 presents the data misfits for different methods. As can be seen from the figure, the
686 RMS values of the clustered mean model and the global mean model are slightly higher than
687 those of the Occam's and PhyDnn inversions. However, the RMS of the best-fitting model and
688 the remaining models within the ensemble are basically comparable to those of the Occam's
689 inversion. This indicates that our Swi-DREI has achieved sufficient convergence, and the
690 ensemble models possess high credibility.

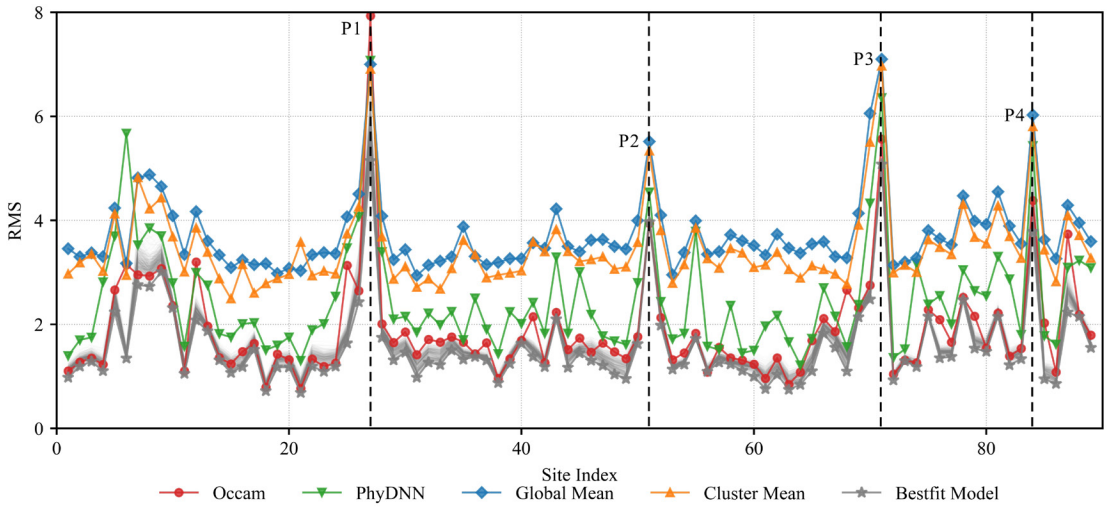



**Figure. 17** RMSs for five survey lines. The gray shaded region represents the RMS distribution interval of the posterior model ensemble. P1–P4 indicate outlier measurement stations within the survey area characterized by substantial data residuals.

Fig. 18 further compares the inversion results at four outlier measurement stations with large data residuals. Among them, Panels (a)–(d) display the single-station inversion results, the posterior resistivity distributions, and RMS histograms respectively for Swi-DREI, PhyDnn, and the Occam's inversion (refer to supplementary materials Fig. S12–S15 for the data fittings). At station P1 (Fig. 18a), the Swi-DREI yields the smallest RMS among the three methods. The posterior distribution map reveals that Occam's inversion exhibits significant fluctuations with multiple oscillations, and the resistivity values in the deep formations are biased to low values. Nevertheless, in the shallow and middle high-resistivity layers, the three methods demonstrate high consistency, the posterior distribution range provided by Swi-DREI falls within a reasonable interpretation interval. The subsurface geoelectrical structures at stations P2 and P3 are similar (see Fig. 18b and 18c), where Occam's inversion identifies two high-resistivity layers. At station P2, the shallow high-resistivity layer from the PhyDnn inversion exhibits a smaller burial depth. The high-resistivity layer from Swi-DREI aligns closely with the Occam's results, although the resistivities are lower. For the second high-resistivity layer in the middle section, neither PhyDnn nor Swi-DREI have reconstructed it. The posterior distribution of Swi-DREI remains narrow in the shallow region and gets gradually broadened with depth, indicating that the deep structure is weakly constrained by the data, so the uncertainty increases. At station

P3, all three methods respond to the shallow high-resistivity layer, and the posterior distribution of Swi-DREI widens significantly for this horizon, reflecting the existence of a high-resistivity anomaly accompanied by higher uncertainty. For the middle high-resistivity layer, the PhyDnn response exhibits a larger amplitude, and the posterior distribution of Swi-DREI also shifts toward higher resistivity at this location. At station P4 (Fig. 18d), the results of the three inversions are consistent. However, influenced by the smoothness constraint, Occam's inversion displays distinct low-resistivity region near the high-resistivity layer. whereas the inverted profiles of PhyDnn and Swi-DREI appear smoother and more stable. Summarizing the above discussions, we find that compared with conventional deep learning methods that perform second-level inference, our Swi-DREI method provides more robust inversion results and statistical inferences without significantly increasing computational costs. The provided posterior distributions offer a physically reasonable range for electrical variations and regions of high uncertainty. Furthermore, this method eliminates the need to construct complex training datasets in advance, demonstrating superior flexibility and universality in practical applications.

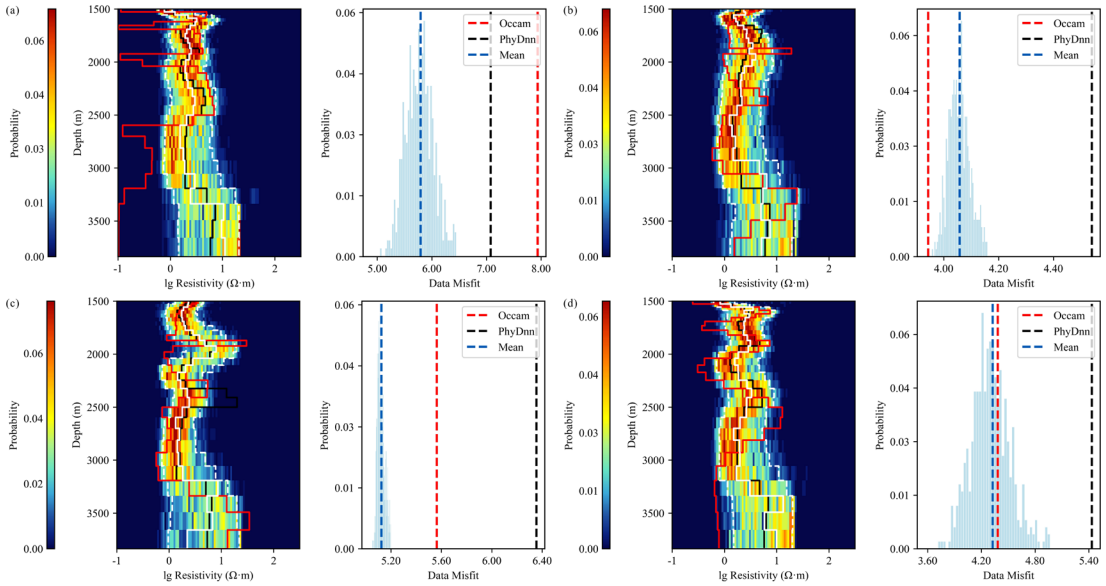



**Figure. 18** Posterior resistivity distributions, single station inversion profiles, and RMS histograms at four outlier stations P1–P4. Panels (a)–(d) correspond to stations P1–P4, respectively. The red lines represent the Occam's inversion, the black lines represent the physics-driven deep learning inversions, while the white lines represent the clustered mean model of the proposed inversion.

## 5. Conclusions

Although the MCSEM method possesses significant advantages in detecting subsurface high-resistivity reservoirs, its inversion process faces severe non-linearity and non-uniqueness due to the weak EM signal and limited data coverage. To address the high computational cost of conventional Bayesian methods and the difficulty of variational inference in preserving correlations among deep-network parameters, we developed a physics-driven deep-ensemble reparameterization framework. This inversion scheme not only provides efficient non-Bayesian approximate inference for geophysical EM inverse problems but also delivers fine-scale imaging and uncertainty estimation of resistivity structure.

The numerical experiment with both synthetic and field survey data confirmed that (1) the developed inversion framework eliminates the dependence on massive external training datasets. Through the implicit regularizations of the deep SwiGLU network, the framework retains the sharpness of physical boundaries of geological anomalies. Meanwhile, it leverages an independent parallel deep ensemble strategy to overcome the limitation in traditional uncertainty evaluations and achieve efficient uncertainty quantification at a low computational cost. (2) Targeting the limitation where the global arithmetic averaging in traditional posterior inference suppresses the amplitude of high-resistivity thin layers and artificially stretches their thicknesses, the proposed joint selection mechanism based on unsupervised clustering and global interface probability has demonstrated its effectiveness in identifying different cluster categories within the model space, objectively isolating the optimal model subset characterized by clear physical boundaries and the highest self-consistency from the equivalent solution ensemble. (3) The proposed algorithm can also maintain high robustness and generalization capabilities under extreme observational conditions. Our deep ensemble reparameterization framework exhibits high performance even for 20% Gaussian random noise or 45% random data missing. The network ensemble can stably reconstruct the macroscopic geoelectrical structures and precisely map the weakly data-constrained regions via standard deviation models, and effectively suppress the non-physical artifacts common in deterministic inversions. (4) Application of the proposed method to a field dataset yields favorable results. Without

introducing explicit regularizations, our method can provide a high-resolution, spatially coherent quasi-3D geological profile. The reconstructed electrical structure aligns closely with the known Cenozoic sedimentary sequence in the survey area. The spatial distributions of the basement and Paleocene marine mudstones have been successfully revealed, while the logarithmic standard deviation and interface probability profiles offer rigorous quantitative statistics for the evaluation of deep targets.

## Appendix A Network Architecture and hyperparameters

To address the characteristics of MCSEM, we adopt a multilayer perceptron generator network driven by Swish-Gated Linear Units (SwiGLU) (Shazeer 2020). A primary challenge in MCSEM exploration arises from the severe imbalance in sensitivity distributions. Whereas the EM fields are highly sensitive to shallow formations, but they decay exponentially outwards to deep high-resistivity targets. During the backpropagation within the conventional neural network, the large gradients generated by parameters associated with shallow formations frequently obscure the updates required for weak deep responses. The dual-branch gating multiplication mechanism in SwiGLU acts as a dynamic adaptive preconditioner within the network architecture. This mechanism actively suppresses overfitting to shallow features and concentrates the non-linear mapping capacity on weak responses from high-resistivity layers at depth, thereby enhancing the characterization to deep reservoirs. Additionally, the SwiGLU is smooth and continuously differentiable across the entire domain, thereby mitigating the dead-neuron problem and stagnation during the iterative optimizations frequently induced by the conventional rectified linear unit (ReLU) functions. This ensures unimpeded gradient flow across all depths when exploring complex solution spaces and guarantees the parallel convergence of multiple individual models.

As illustrated in Fig. A1A, the input to the ensemble system comprising $N$ parallel models consists of Gaussian random vectors or prior geological information. The forward propagation of the network involves three stages. The first is the input mapping layer, where the input vectors are projected onto a high-dimensional latent space $h$ via independent ensemble linear layers and undergo initial feature extraction using the SiLU (Sigmoid Linear Unit) activation

function. The second stage is the layer for main feature extraction, which employs $L$ cascaded gated residual blocks to perform high-dimensional non-linear mappings. This stage delineates the spatial correlation among inverted parameters while maintaining the dimension $h$ constant. The third stage is the output mapping layer, where the fully extracted features enter a tail module and are mapped back to the physical model space through sequential linear projections from h to $h/2$, and ultimately to $d_{out}$. Depending on the physical properties of the parameters within the output layer, such as the logarithmic bounds governing resistivity, specific activation functions are applied to yield the final one-dimensional geoelectrical model. Specifically, a Sigmoid function is utilized for direct input and warm-up strategies, whereas a linear function is employed for the perturbation prediction strategy.

Fig. A1B illustrates the mathematical framework of the core modules. To ensure strict independence among $N$ ensemble members during the parallel computation, all underlying operators of the network are rewritten. Unlike the fully connected layers in conventional method, the weights and biases of the ensemble linear layers remain unshared across the batch dimension $N$, and the forward propagation is achieved through batched matrix multiplication. This design ensures that each model maintains a completely independent parameter trajectory while sharing the overall architecture, thereby preserving the diversity of the ensemble throughout the inversion process. To mitigate the vanishing gradient problem in deep networks and accelerate convergence, a layer normalization scheme is introduced into the architecture. The mean and variance are calculated independently across the feature channels of each individual model, and thus ensuring the stability of the optimization trajectory. The gating mechanism of SwiGLU serves as the core non-linear activation unit within the residual blocks. In contrast to conventional processing using ReLU functions, the input features are first expanded to a dimension of $2h$ via a linear layer and subsequently divided equally along the channel dimension into a Value branch ($\mathbf{V}$) and a Gate branch ($\mathbf{G}$). The final activation output is computed non-linearly through a Hadamard product, representing element-wise multiplication, which can be expressed as

$$\text{Output} = \mathbf{V} \odot \text{SiLU}(\mathbf{G}) . \tag{A1}$$

This mechanism enables the network architecture to dynamically suppress noise and augment the capacity to fit weak anomalous responses in MCSEM data. The residual blocks employ pre-normalization architecture and layer normalization prior to any affine transformation or non-linear activation. Combined with residual connections, this constructs a direct gradient channel and guarantees stable gradient propagation across complex loss landscapes.

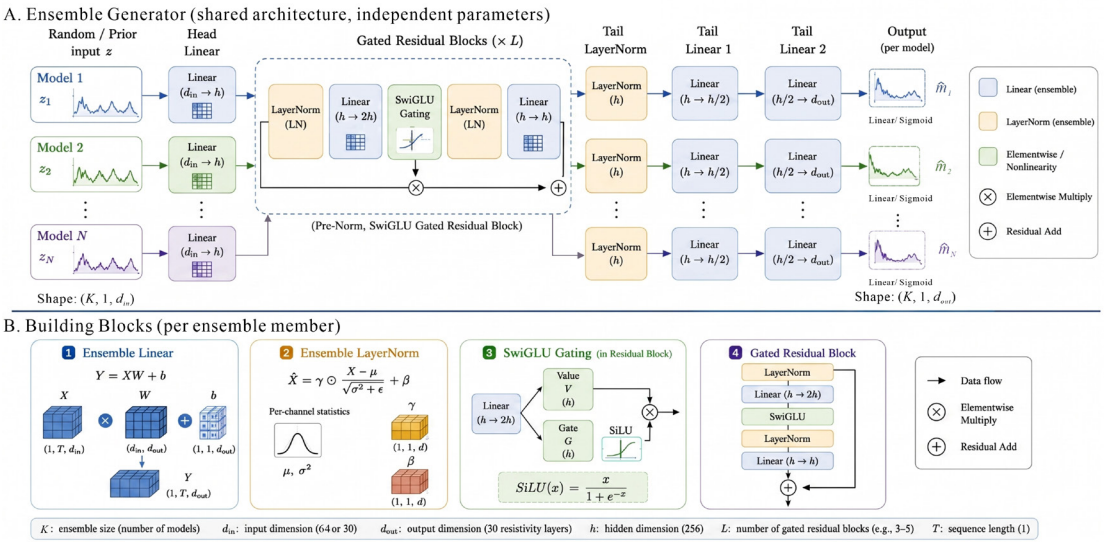



**Figure. A1** Schematic diagram of Swi-DREI network architecture. In this study, the ensemble size $K$ is set to 500, and the number of gated residual blocks is set to 3 (This parameter can be adjusted based on the dimensionality of the inverse problem or data complexity). For different input schemes, the input dimension for the perturbation prediction strategy is set to 64, corresponding to the length of the random noise sequence, while the input dimension for the warm-up strategy is set to 30, corresponding to the spatial dimension of the prior model.

## Appendix B Field data results

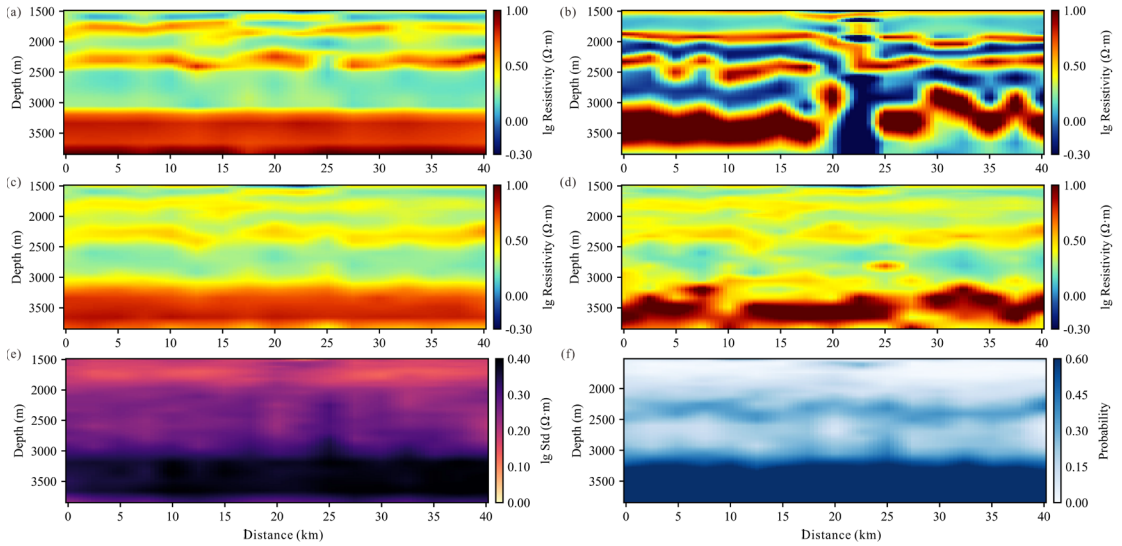



**Figure. B1** Inversion results for Survey Line 2 using the perturbation strategy. (a) Physics-driven deep learning inversion; (b) Occam's inversion; (c) Swi-DREI global mean model; (d) Swi-DREI clustered mean model; (e) global logarithmic standard deviation; (f) global interface probability.

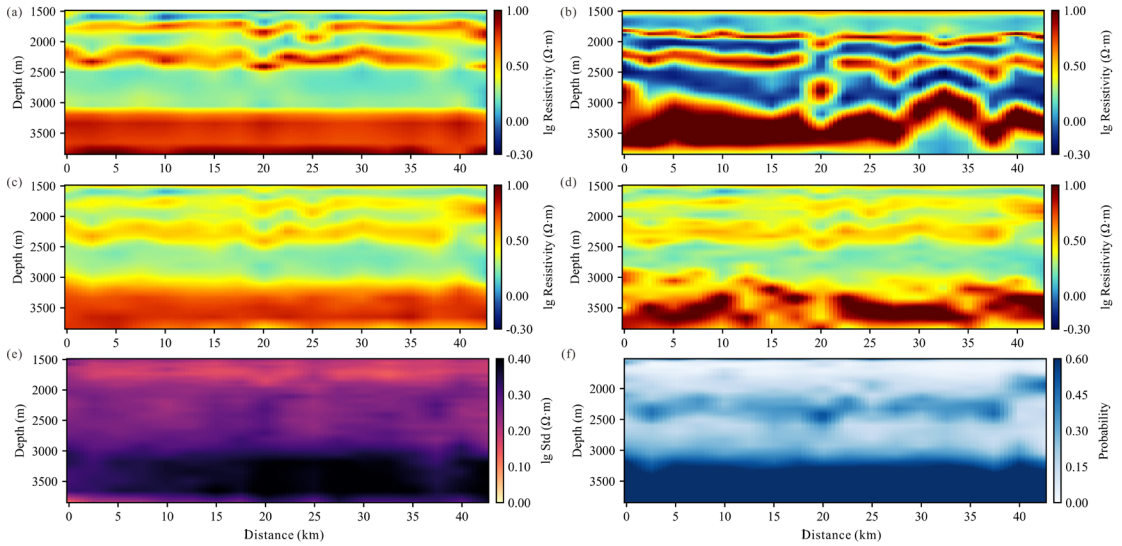
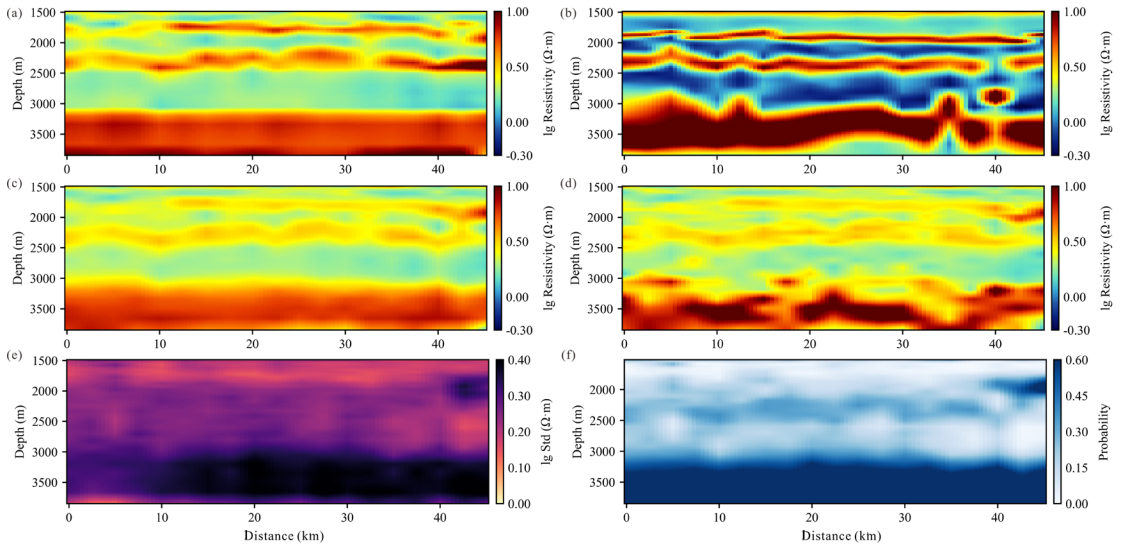
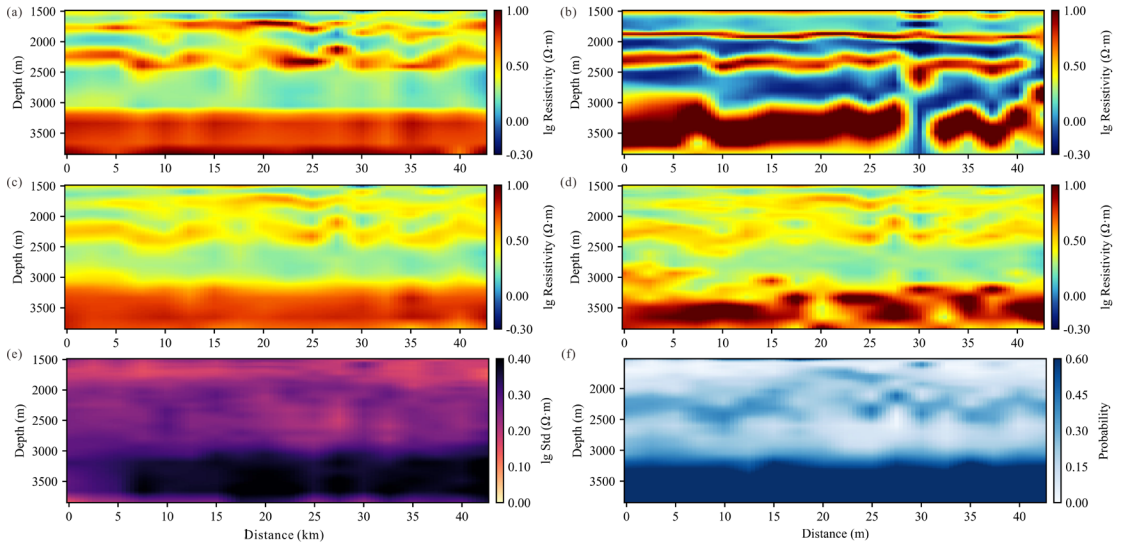



**Figure. B2** Inversion results for Survey Line 3 using the perturbation strategy. (a) Physics-driven deep learning inversion; (b) Occam's inversion; (c) Swi-DREI global mean model; (d) Swi-DREI clustered mean model; (e) global logarithmic standard deviation; (f) global interface probability.




840

841 **Figure. B3** Inversion results for Survey Line 4 using the perturbation strategy. (a) Physics-
842 driven deep learning inversion; (b) Occam's inversion; (c) Swi-DREI global mean model; (d)
843 Swi-DREI clustered mean model; (e) global logarithmic standard deviation; (f) global interface
844 probability.




845

846 **Figure. B4** Inversion results for Survey Line 5 using the perturbation strategy. (a) Physics-
847 driven deep learning inversion; (b) Occam's inversion; (c) Swi-DREI global mean model; (d)
848 Swi-DREI clustered mean model; (e) global logarithmic standard deviation; (f) global interface
849 probability.

850 **Acknowledgements**

851 This research was jointly supported by the National Natural Science Foundation of China under
852 Grant Nos. 42530804, 42522405, 42274093 and 42074120.

## Data Availability

The data that support the findings of this study are available from the corresponding author upon reasonable request.

## Reference


Ahmed, A., Aigner, L., Michel, H., Deleersnyder, W., Dudal, D., Flores Orozco, A., Hermans, T., 2024. Assessing and Improving the Robustness of Bayesian Evidential Learning in One Dimension for Inverting Time-Domain Electromagnetic Data: Introducing a New Threshold Procedure. Water 16, 1056. https://doi.org/10.3390/w16071056

Blei DM, Kucukelbir A, McAuliffe JD (2017) Variational Inference: A Review for Statisticians. Journal of the American Statistical Association 112:859–877. https://doi.org/10.1080/01621459.2017.1285773

Buland A, Kolbjørnsen O (2012) Bayesian inversion of CSEM and magnetotelluric data. Geophysics 77:E33–E42. https://doi.org/10.1190/geo2010-0298.1

Cheng Z, Gadelha M, Maji S, Sheldon D (2019) A Bayesian Perspective on the Deep Image Prior. In: Proceedings of the IEEE/CVF Conference on Computer Vision and Pattern Recognition (CVPR)

Constable S (2010) Ten years of marine CSEM for hydrocarbon exploration. Geophysics 75:75A67-75A81. https://doi.org/10.1190/1.3483451

Constable SC, Parker RL, Constable CG (1987) Occam's inversion; a practical algorithm for generating smooth models from electromagnetic sounding data. Geophysics 52:289–300. https://doi.org/10.1190/1.1442303

Dhara A, Sen M (2022) Elastic-AdjointNet: A physics-guided deep autoencoder to overcome crosstalk effects in multiparameter full-waveform inversion. In: Second International Meeting for Applied Geoscience & Energy. Society of Exploration Geophysicists and American Association of Petroleum Geologists, Houston, Texas, pp 882–886

Fichtner A, Bunge H-P, Igel H (2006) The adjoint method in seismology. Physics of the Earth and Planetary Interiors 157:86–104. https://doi.org/10.1016/j.pepi.2006.03.016

880 Folgoc LL, Baltatzis V, Desai S, et al (2021) Is MC Dropout Bayesian? arXiv preprint
881 arXiv:2110.04286
882 Fort S, Hu H, Lakshminarayanan B (2019) Deep Ensembles: A Loss Landscape Perspective.
883 arXiv preprint arXiv:1912.02757
884 Gal Y, Ghahramani Z (2016) Dropout as a Bayesian Approximation: Representing Model
885 Uncertainty in Deep Learning. In: Balcan MF, Weinberger KQ (eds) Proceedings of The
886 33rd International Conference on Machine Learning. PMLR, New York, New York,
887 USA, pp 1050–1059
888 Grayver A (2024) Unravelling the Electrical Conductivity of Earth and Planets. Surv Geophys
889 45:187–238. https://doi.org/10.1007/s10712-023-09813-9
890 Guo R, Zhou H, Wei X, et al (2025) Deep joint inversion of multiple geophysical data with U-
891 net reparameterization. Geophysics 90:WA61–WA75. https://doi.org/10.1190/geo2024-
892 0210.1
893 Guo Z, Xue G, Liu J, Wu X (2020) Electromagnetic methods for mineral exploration in China:
894 A review. Ore Geology Reviews 118:103357.
895 https://doi.org/10.1016/j.oregeorev.2020.103357
896 Hansen, T.M., Finlay, C.C., 2022. Use of Machine Learning to Estimate Statistics of the
897 Posterior Distribution in Probabilistic Inverse Problems—An Application to Airborne
898 EM Data. JGR Solid Earth 127, e2022JB024703.
899 https://doi.org/10.1029/2022JB024703
900 He Q, Wang Y (2021) Reparameterized full-waveform inversion using deep neural networks.
901 Geophysics 86:V1–V13. https://doi.org/10.1190/geo2019-0382.1
902 Huang Q, Wu S, Xue J (2026) Data Science and Machine Learning in Geo-Electromagnetics:
903 A Review. Surv Geophys 47:677–732. https://doi.org/10.1007/s10712-025-09904-9
904 Izmailov P, Vikram S, Hoffman MD, Wilson AGG (2021) What Are Bayesian Neural Network
905 Posteriors Really Like? In International Conference on Machine Learning. PMLR, pp
906 4629–4640

Karniadakis GE, Kevrekidis IG, Lu L, et al (2021) Physics-informed machine learning. Nat Rev Phys 3:422–440. https://doi.org/10.1038/s42254-021-00314-5

Key K (2012) Marine Electromagnetic Studies of Seafloor Resources and Tectonics. Surv Geophys 33:135–167. https://doi.org/10.1007/s10712-011-9139-x

Key K (2009) 1D inversion of multicomponent, multifrequency marine CSEM data: Methodology and synthetic studies for resolving thin resistive layers. Geophysics 74:F9–F20. https://doi.org/10.1190/1.3058434

Key K (2016) MARE2DEM: a 2-D inversion code for controlled-source electromagnetic and magnetotelluric data. Geophys J Int 207:571–588. https://doi.org/10.1093/gji/ggw290

Kingma, D. P., Ba, J. (2014) Adam: A method for stochastic optimization. arXiv preprint arXiv:1412.6980

Lakshminarayanan B, Pritzel A, Blundell C (2017) Simple and Scalable Predictive Uncertainty Estimation using Deep Ensembles. Advances in Neural Information Processing Systems.

Li G, Liu Y, Castillo-Reyes O (2026a) Recent Advances in 2D Frequency-Domain Marine Controlled-Source EM Inversion Using Adjoint Approximate Sensitivities. Surv Geophys 47:85–108. https://doi.org/10.1007/s10712-025-09925-4

Li Z, Li H, Li K, Beshr AM (2026) TorchTEM3D: PyTorch-Driven forward modeling platform for fast 3D transient electromagnetic modeling and efficient sensitivity matrix calculation. Computers & Geosciences 207:106063. https://doi.org/10.1016/j.cageo.2025.106063

Liang H, Gao R, Yin C, et al (2024) Physics-driven deep-learning for marine CSEM data inversion. Journal of Applied Geophysics 229:105474. https://doi.org/10.1016/j.jappgeo.2024.105474

Liu F, Li H, Zou G, Li J (2025) Automatic Differentiation-Based Full Waveform Inversion With Flexible Workflows. Journal of Geophysical Research: Machine Learning and Computation 2:e2024JH000542. https://doi.org/10.1029/2024JH000542

933 Liu F, Li Y-X, Su R, et al (2026a) Deep reparameterization for full waveform inversion:
934 Architecture benchmarking, robust inversion, and multiphysics extension. Petroleum
935 Science 23:1890–1907. https://doi.org/10.1016/j.petsci.2025.12.027

936 Liu M, Grana D, Mosegaard K, et al (2026b) Bayesian Inference for Subsurface Geophysical
937 Inverse Problems. Reviews of Geophysics 64:e2025RG000884.
938 https://doi.org/10.1029/2025RG000884

939 Liu Y, Ma X, Wang L, et al (2024) A Robust Approach for Geo-Electromagnetic Sounding Data
940 Inversion Using l1 -Norm Misfit and Adaptive Moment Estimation. IEEE Trans Geosci
941 Remote Sensing 62:1–12. https://doi.org/10.1109/TGRS.2024.3396080

942 Liu Y, Yin C, Qiu C, et al (2019) 3-D inversion of transient EM data with topography using
943 unstructured tetrahedral grids. Geophysical Journal International 217:301–318.
944 https://doi.org/10.1093/gji/ggz014

945 Minsley BJ (2011) A trans-dimensional Bayesian Markov chain Monte Carlo algorithm for
946 model assessment using frequency-domain electromagnetic data: Bayesian MCMC
947 algorithm for model assessment. Geophysical Journal International 187:252–272.
948 https://doi.org/10.1111/j.1365-246X.2011.05165.x

949 Michel, H., Hermans, T., Nguyen, F., 2022. Iterative prior resampling and rejection sampling
950 to improve 1-D geophysical imaging based on Bayesian evidential learning (BEL1D).
951 Geophysical Journal International 232, 958–974. https://doi.org/10.1093/gji/ggac372

952 Mosegaard K, Tarantola A (1995) Monte Carlo sampling of solutions to inverse problems. J
953 Geophys Res 100:12431–12447. https://doi.org/10.1029/94JB03097

954 Osband I, Blundell C, Pritzel A, Van Roy B (2016) Deep Exploration via Bootstrapped DQN.
955 Advances in Neural Information Processing Systems.

956 Ovadia Y, Fertig E, Ren J, et al (2019) Can You Trust Your Model's Uncertainty? Evaluating
957 Predictive Uncertainty Under Dataset Shift. Advances in neural information processing
958 systems.

Rahaman N, Baratin A, Arpit D, et al (2018) On the Spectral Bias of Neural Networks. https://doi.org/10.48550/ARXIV.1806.08734

Raissi M, Perdikaris P, Karniadakis GE (2019) Physics-informed neural networks: A deep learning framework for solving forward and inverse problems involving nonlinear partial differential equations. Journal of Computational Physics 378:686–707. https://doi.org/10.1016/j.jcp.2018.10.045

Ray A, Key K (2012) Bayesian inversion of marine CSEM data with a trans-dimensional self parametrizing algorithm: Trans-dimensional inversion of CSEM data. Geophysical Journal International no-no. https://doi.org/10.1111/j.1365-246X.2012.05677.x

Rudin LI, Osher S, Fatemi E (1992) Nonlinear total variation based noise removal algorithms. Physica D: Nonlinear Phenomena 60:259–268. https://doi.org/10.1016/0167-2789(92)90242-F

Sambridge M, Rickwood P, Rawlinson N, Sommacal S (2007) Automatic differentiation in geophysical inverse problems. Geophysical Journal International 170:1–8. https://doi.org/10.1111/j.1365-246X.2007.03400.x

Sen MK, Stoffa PL (2013) Global Optimization Methods in Geophysical Inversion, 2nd edn. Cambridge University Press

Shazeer N (2020) GLU variants improve transformer. arXiv preprint arXiv:200205202

Su Y, Yin C, Liu Y, et al (2022) Sparse-Promoting 3-D Airborne Electromagnetic Inversion Based on Shearlet Transform. IEEE Trans Geosci Remote Sensing 60:1–13. https://doi.org/10.1109/TGRS.2021.3061160

Sun J, Innanen K, Zhang T, Trad D (2023) Implicit Seismic Full Waveform Inversion With Deep Neural Representation. JGR Solid Earth 128:e2022JB025964. https://doi.org/10.1029/2022JB025964

Tarantola A (2005) Inverse Problem Theory and Methods for Model Parameter Estimation. Society for Industrial and Applied Mathematics

Tikhonov AN, Arsenin VY (1977) Solutions of ill-posed problems. Winston, Washington, DC

Ulyanov D, Vedaldi A, Lempitsky V (2018) Deep Image Prior. In: Proceedings of the IEEE Conference on Computer Vision and Pattern Recognition (CVPR)

Wang F, Huang X, Alkhalifah TA (2023) A Prior Regularized Full Waveform Inversion Using Generative Diffusion Models. IEEE Trans Geosci Remote Sensing 61:1–11. https://doi.org/10.1109/TGRS.2023.3337014

Wang H, Yu S (2024) Regularized Full-Waveform Inversion With Shearlet Transform and Total Generalized Variation. IEEE Trans Geosci Remote Sensing 62:1–15. https://doi.org/10.1109/TGRS.2024.3449244

Wang J, Lan C, Liu C, et al (2022) Generalizing to unseen domains: A survey on domain generalization. IEEE transactions on knowledge and data engineering 35:8052–8072

Wenzel F, Roth K, Veeling BS, et al (2020) How Good is the Bayes Posterior in Deep Neural Networks Really? arXiv preprint arXiv:2002.02405

Xu Z-QJ, Zhang Y, Xiao Y (2019) Training Behavior of Deep Neural Network in Frequency Domain. In: Gedeon T, Wong KW, Lee M (eds) Neural Information Processing. Springer International Publishing, Cham, pp 264–274

Yang F, Liu Y, Yin C, et al (2026) Corrections to “Beyond L2: Leveraging Sinkhorn Distance for Improved Resistivity Recovery in 3-D Magnetotelluric Inversion.” IEEE Trans Geosci Remote Sensing 64:1–1. https://doi.org/10.1109/TGRS.2026.3660388

Yu S, Ma J (2021) Deep Learning for Geophysics: Current and Future Trends. Reviews of Geophysics 59:e2021RG000742. https://doi.org/10.1029/2021RG000742

Zhao D, Zhao F, Gan Y (2020) Reference-Driven Compressed Sensing MR Image Reconstruction Using Deep Convolutional Neural Networks without Pre-Training. Sensors 20:308. https://doi.org/10.3390/s20010308

Zhdanov MS (2010) Electromagnetic geophysics: Notes from the past and the road ahead. Geophysics 75:75A49-75A66. https://doi.org/10.1190/1.3483901

1011 Zhu W, Xu K, Darve E, et al (2022) Integrating deep neural networks with full-waveform
1012 inversion: Reparameterization, regularization, and uncertainty quantification.
1013 Geophysics 87:R93–R109. https://doi.org/10.1190/geo2020-0933.1

**Supporting information for "Efficient Uncertainty Quantification for Marine CSEM via Swi-DREI: A Physics-Driven Deep Reparameterization Ensemble Approach with Implicit Regularization"**

**Contents of this file**

Figures S1-S15

Introduction

This supplementary document compiles auxiliary validation experiments, hyperparameter sensitivity analyses, and single-station data-fitting diagnostics to support the primary methodologies and conclusions presented in the main manuscript. The material compiled herein expands upon the structural characterization capability and numerical stability of the proposed Swi-DREI framework, providing deeper insights into the performance of the algorithm under both controlled synthetic benchmarks and real-world data constraints.

1. Cluster Stability and Optimum Number of Clusters

Figs. S1–S4 display the outcomes of the ablation experiments regarding the number of clusters for the K-means algorithm applied to Model 1, providing a rigorous quantitative justification for selecting ncluster= 5 as the optimal cluster size in the main text. As is observed, when the total count of clusters is small (i.e., 2 or 3), the equivalent models characterized by discrete physical attributes are prematurely forced into a single category, causing the resulting mean models to fail in delivering a satisfactory structural reconstruction. Conversely, when the number of clusters increases to 6, the membership size within certain clusters becomes excessively small, accompanied by redundant physical features, which exhibit an undesirable over-segmentation within the high-dimensional model space. In Section 2, Fig. S9 further compares the distributions of the model ensembles across individual clusters under different inversion strategies. One can see that under both strategies, the individual members within the preferred clusters are tightly distributed around the true geoelectrical profile (represented by the black solid lines), explicitly demonstrating the capacity of the proposed joint selection mechanism to focus the solution space when mitigating the non-uniqueness in the inversions.

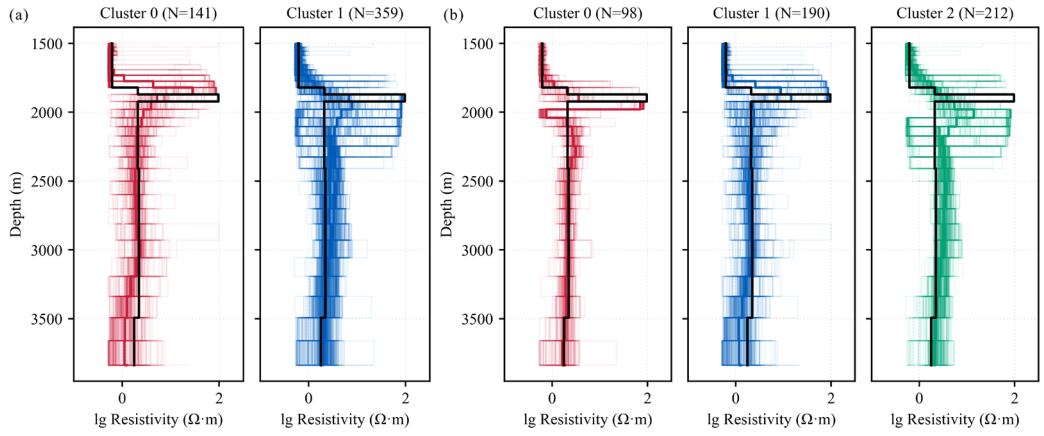



Fig. S1 Clustered mean models derived from the inversion ensemble for Model 1 under the perturbation

prediction strategy with the number of clusters specified as 2 and 3.

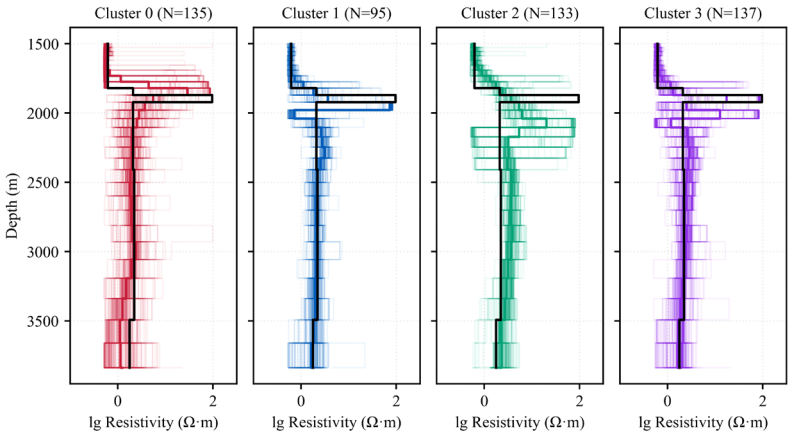



Fig. S2 Clustered mean models derived from the inversion ensemble for Model 1 under the perturbation prediction strategy with the number of clusters specified as 4.

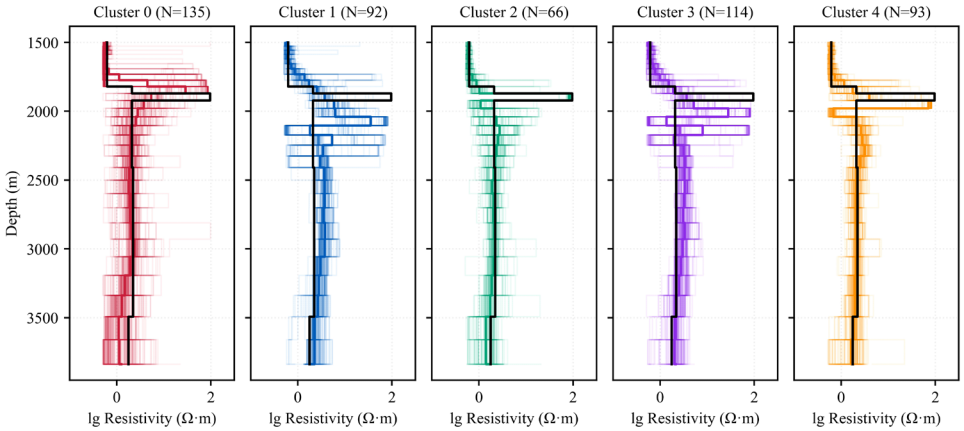



Fig. S3 Clustered mean models derived from the inversion ensemble for Model 1 under the perturbation prediction strategy with the number of clusters specified as 5.

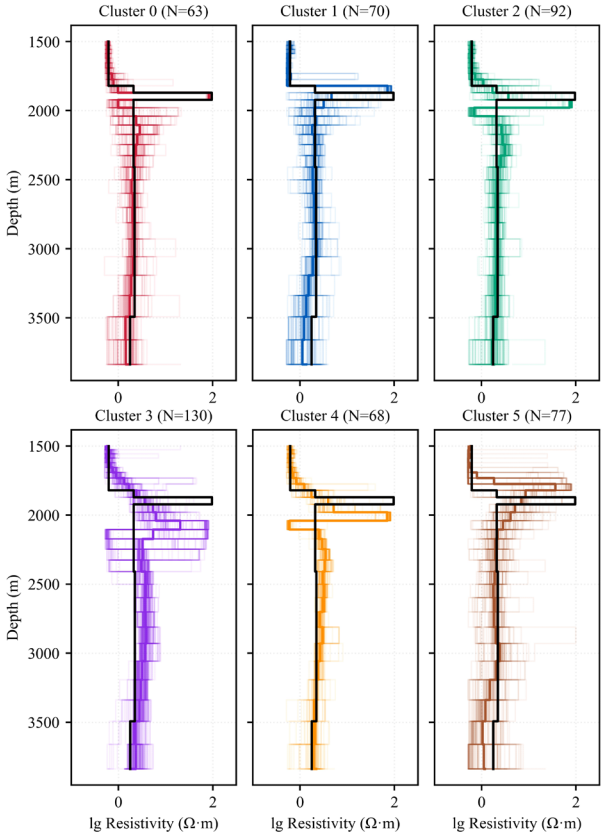



Fig. S4 Clustered mean models derived from the inversion ensemble for Model 1 under the perturbation prediction strategy with the number of clusters specified as 6.

2. Data-Fitting Analysis for Synthetic Models

Figs. S5–S8 provide details of data-fitting characteristics of the developed framework when testing on synthetic data for one-dimensional (1D) reservoir models (Model 1 and Model 2). It can be observed that for the noise-contaminated synthetic data (black solid lines), the forward-modeled curves generated by individual ensemble members (gray solid lines) form a robust envelope, indicating that the optimization trajectories of the ensemble effectively span the equivalent solution space. The electromagnetic (EM) responses corresponding to the best-fitting model (denoted by the purple dashed lines) fit the measured signal well, no discernible bias either for amplitudes or phases occur. This validates the stable convergence characteristic inherent in physics-driven optimization. Furthermore, a comparative analysis between the results for Model 1 and Model 2 reveals that due to the higher resistivity contrast within Model 1, the posterior ensemble contains several models with poor data fitting. However, when directly calculating the global mean, it will be influenced by these outlier samples. The cluster mean scheme can effectively mitigate this limitation. Figs. S5–S9 give the details.

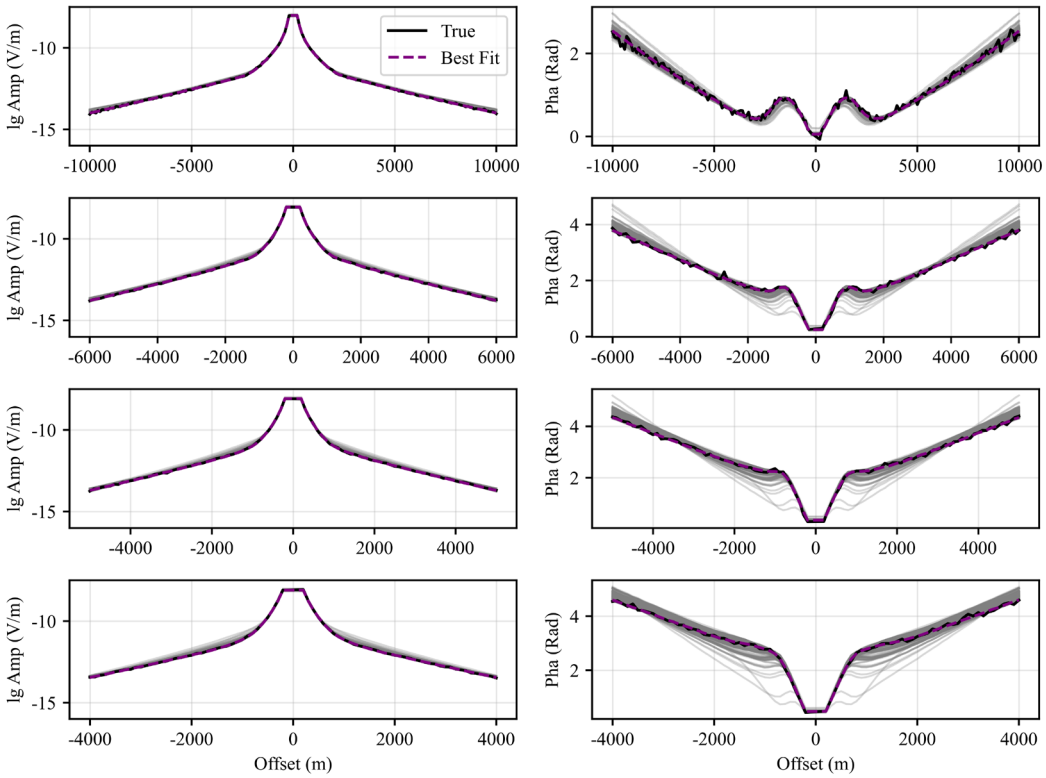



Fig. S5 Data-fitting results obtained through the perturbation prediction strategy for Model 1. The black solid lines represent the noise-contaminated synthetic responses, the purple dashed lines denote the responses corresponding to the best-fitting model, and the gray solid lines illustrate the response curves generated by all individual members within the ensemble.

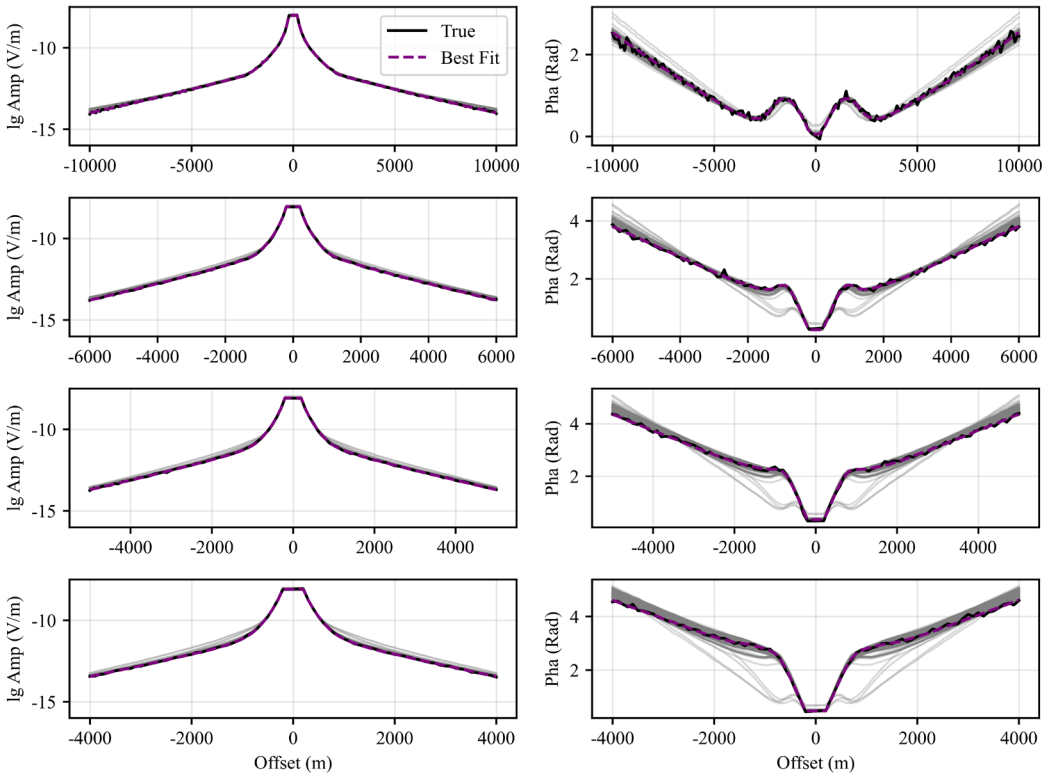



Fig. S6 Data-fitting results obtained through the warm-up training strategy for Model 1. The black solid

lines represent the noise-contaminated synthetic responses, the purple dashed lines denote the responses corresponding to the best-fitting model, and the gray solid lines illustrate the response curves generated by all individual members within the ensemble.

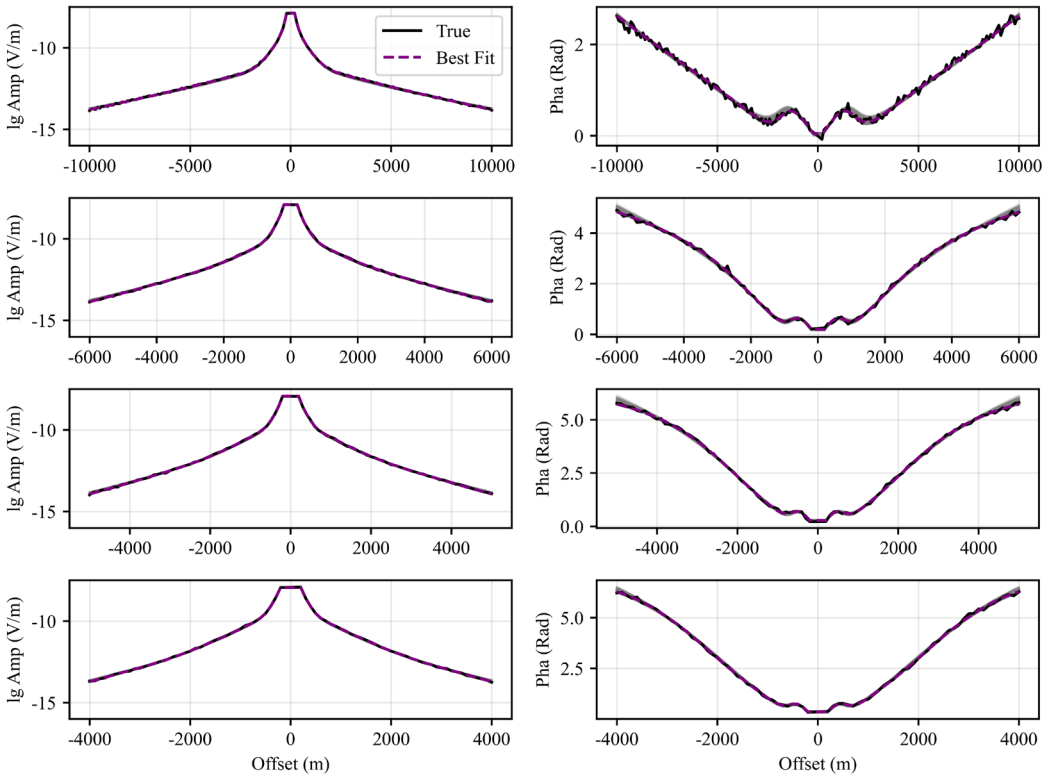



Fig. S7 Data-fitting results obtained through the perturbation prediction strategy for Model 2. The black solid lines represent the noise-contaminated synthetic responses, the purple dashed lines denote the responses corresponding to the best-fitting model, and the gray solid lines illustrate the response curves generated by all individual members within the ensemble.

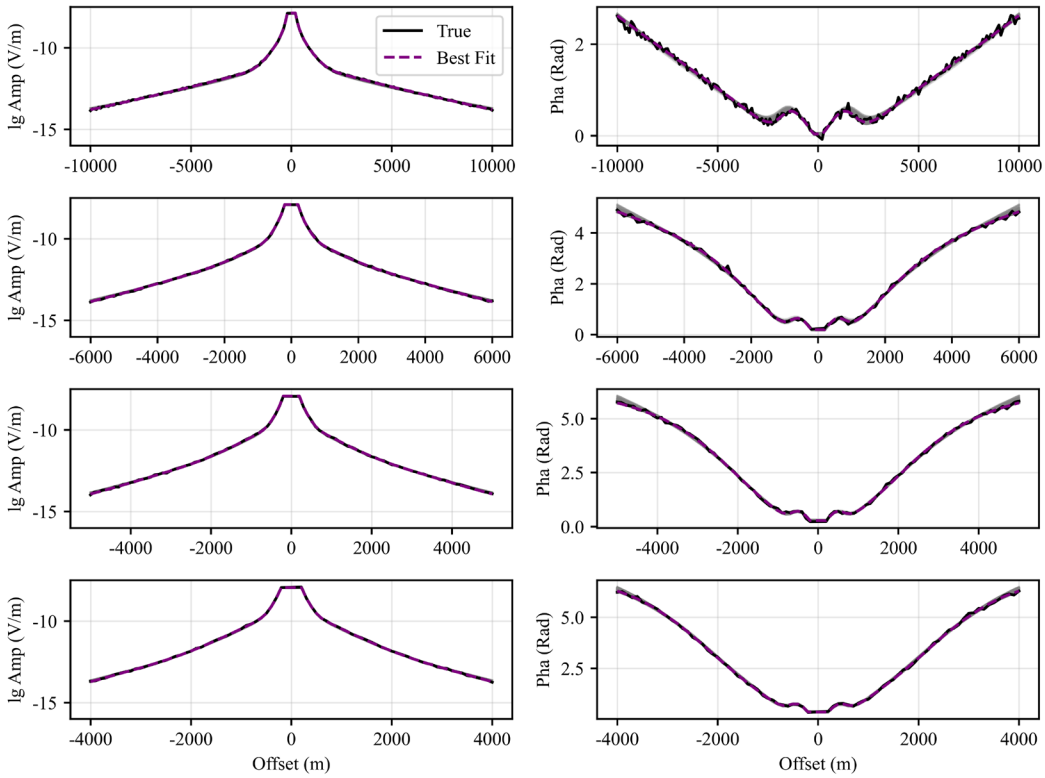



Fig. S8 Data-fitting results obtained through the warm-up training strategy for Model 2. The black solid lines represent the noise-contaminated synthetic responses, the purple dashed lines denote the responses corresponding to the best-fitting model, and the gray solid lines illustrate the response curves generated by all individual members within the ensemble

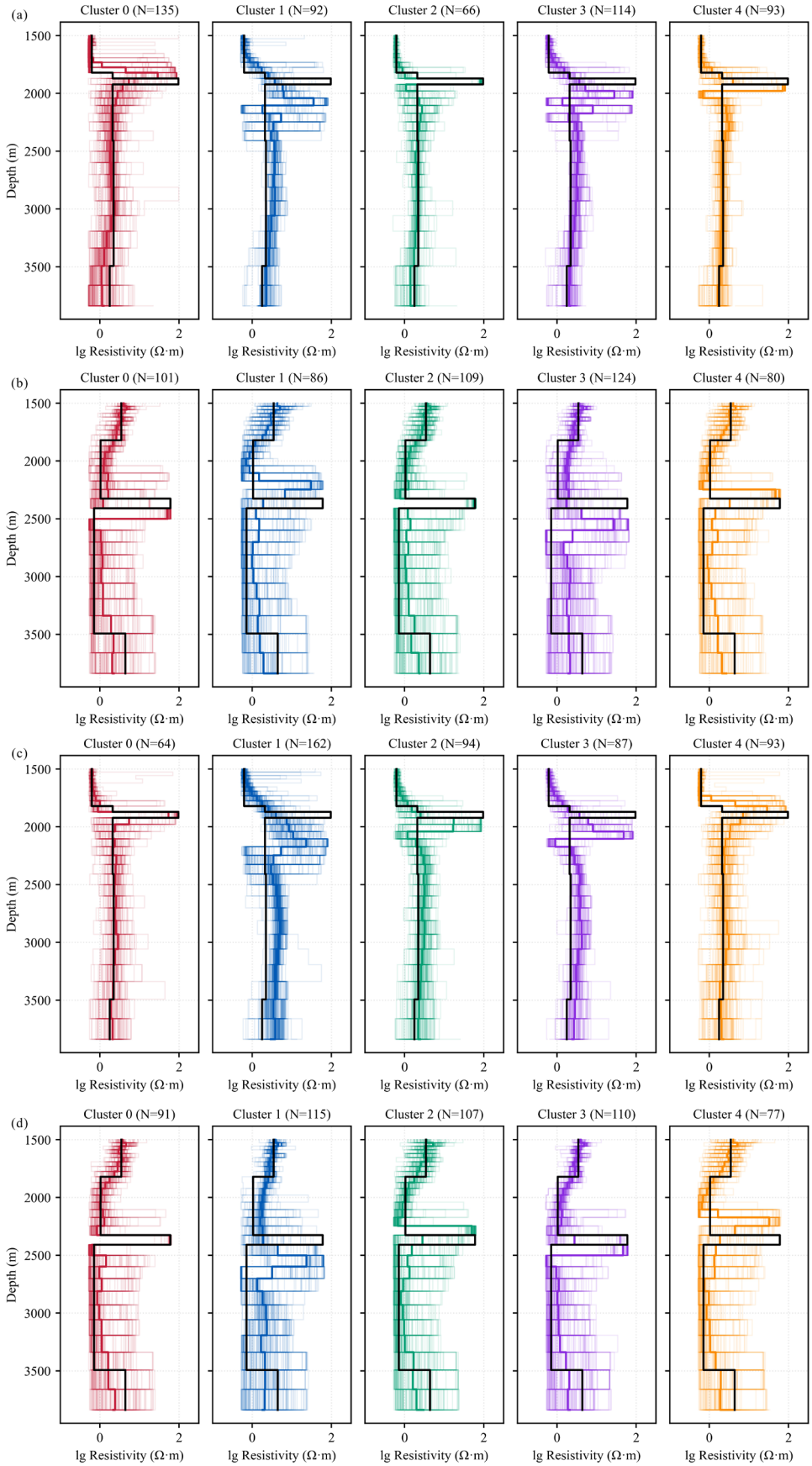



**Fig. S9** Clustered inversion model ensembles partitioned via the K-means algorithm. Subplots a and b present the categories of models for Model 1 and Model 2 under the perturbation prediction strategy,

respectively, whereas subplots c and d illustrate those under the warm-up training strategy. The black solid lines denote the true geoelectrical profiles, and the other colored lines describe the individual model distributions and their corresponding cluster means across discrete subsets.

3. Supplementary Results for Robustness Tests

Similar to the perturbation prediction strategy detailed in the main text, the global mean models obtained via the warm-up training strategy (illustrated in the right column of Fig. S10) remain capable of resolving macro-scale geological structures under high noise levels. However, their ability to resolve thin-layer targets relies more on the joint selection mechanism. Moreover, similar to the best-fitting model in noise testing, the resistivity profiles derived from single individual models in Fig. S11 show poor spatial continuity. As the ratio of missing data gradually increases, the unphysical voids emerge within the core anomalous area, and the delineated interface of the high-resistivity basement exhibits oscillations.

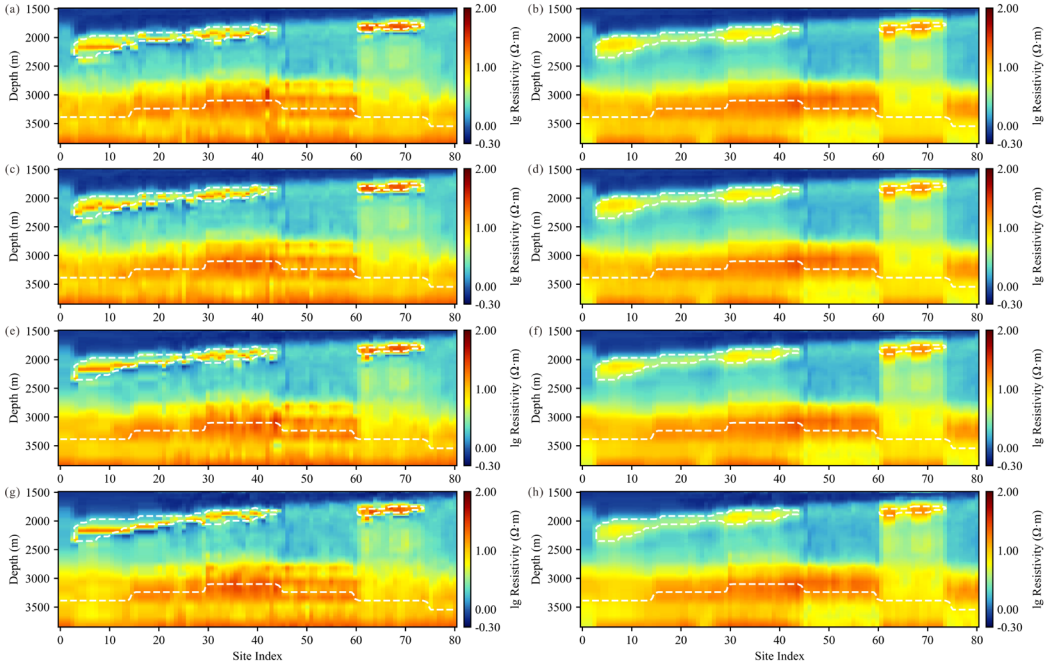



**Fig. S10** Inverted resistivity profiles for the 2D salt dome model obtained through the warm-up training strategy under varying noise levels. From the top to the bottom rows, the four rows correspond to noise ratios of 1%, 5%, 10%, and 20%, respectively. The left column displays the clustered mean models, while the right column shows the global mean models.

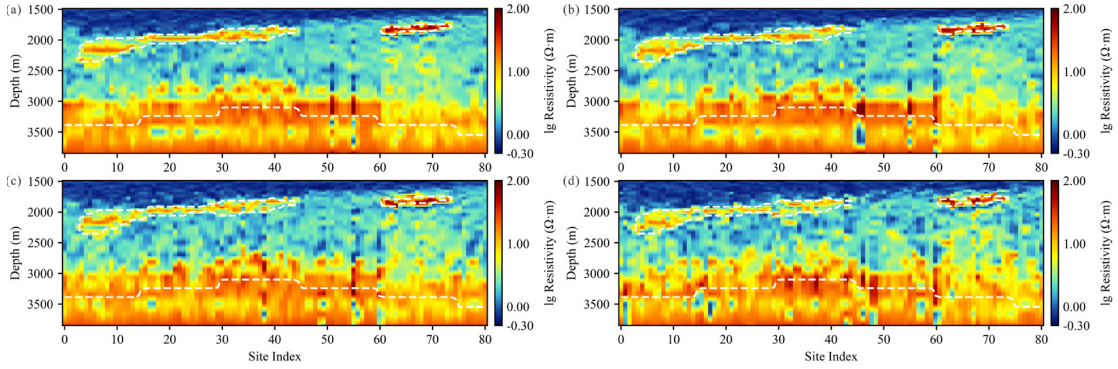



**Fig. S11** Best-fitting individual models within the ensemble under the perturbation prediction strategy.

Subplots a, b, c, and d correspond to data missing ratios of 0%, 15%, 35%, and 45%, respectively.

4. Comparisons of Data-Fitting for Outlier Stations

Figs.S12-S15 shows the data fitting for the perturbation prediction strategy at survey station P1-P4. It is seen that the field data acquired at each station (black solid lines) are effectively fitted by both the individual members within the Swi-DREI ensemble and the corresponding best-fitting model (red dashed lines). As for the phase fitting at Station P3, all inversion methods, including the Occam's inversion and the PhyDnn inversion exhibit a systematic discrepancy at specific transmitting frequencies, which indicates the presence of a possible localized lateral heterogeneity or uncalibrated instrument noise inherent in the survey environment, and thus highlighting the necessity to evaluate uncertainty during field data interpretation.

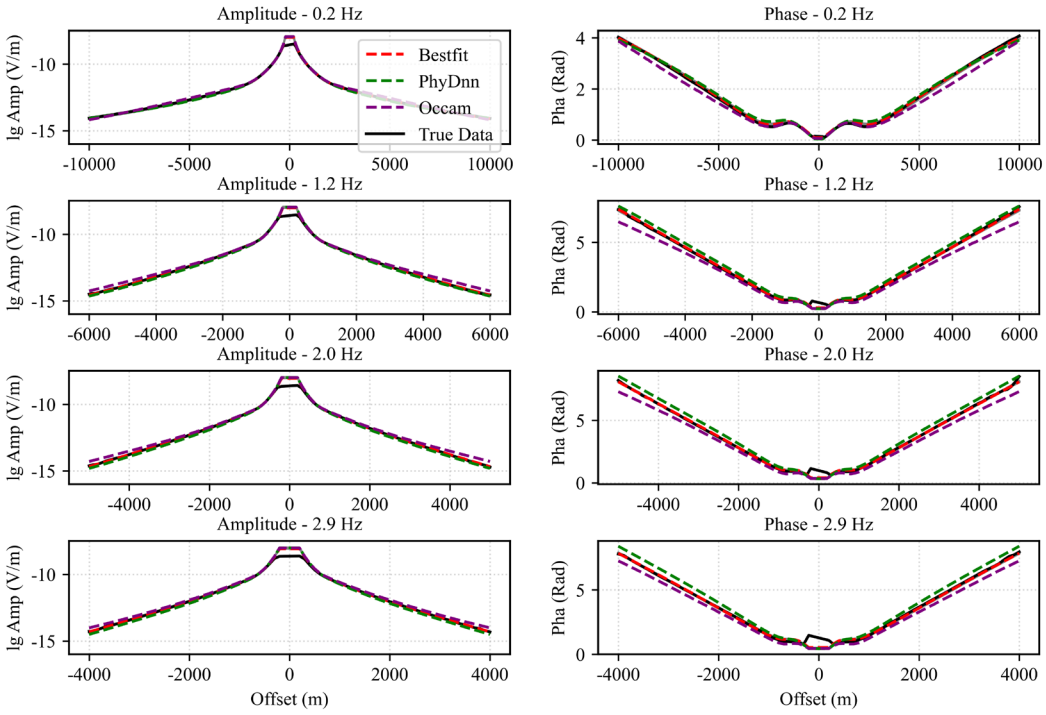



**Fig. S12** Data-fitting curves at Station P1 obtained through the perturbation prediction strategy. The black solid lines represent the data observations, the red dashed lines denote the responses corresponding to the best-fitting model, and the gray solid lines illustrate the curves generated by individual ensemble members. The green dashed lines indicate the electromagnetic responses computed from the PhyDnn, whereas the purple dashed lines represent those yielded by the conventional Occam inversion.

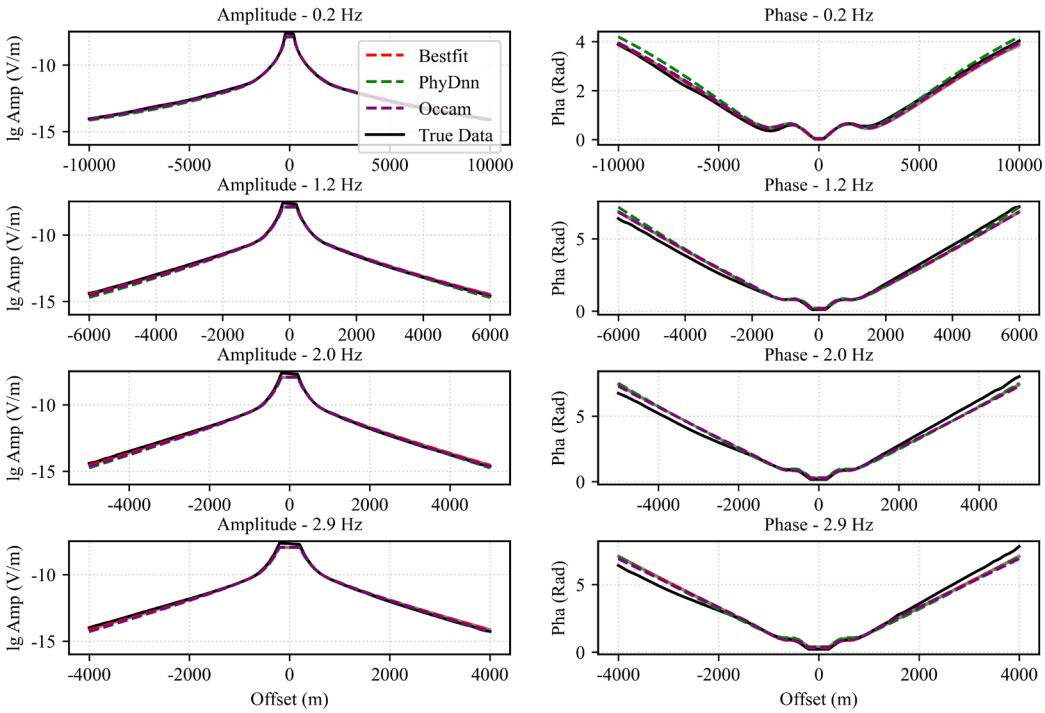



**Fig. S13** Data-fitting curves at Station P2 obtained through the perturbation prediction strategy. The black solid lines represent the data observations, the red dashed lines denote the responses corresponding to the best-fitting model, and the gray solid lines illustrate the curves generated by individual ensemble members. The green dashed lines indicate the electromagnetic responses computed from the PhyDnn, whereas the purple dashed lines represent those yielded by the conventional Occam inversion.

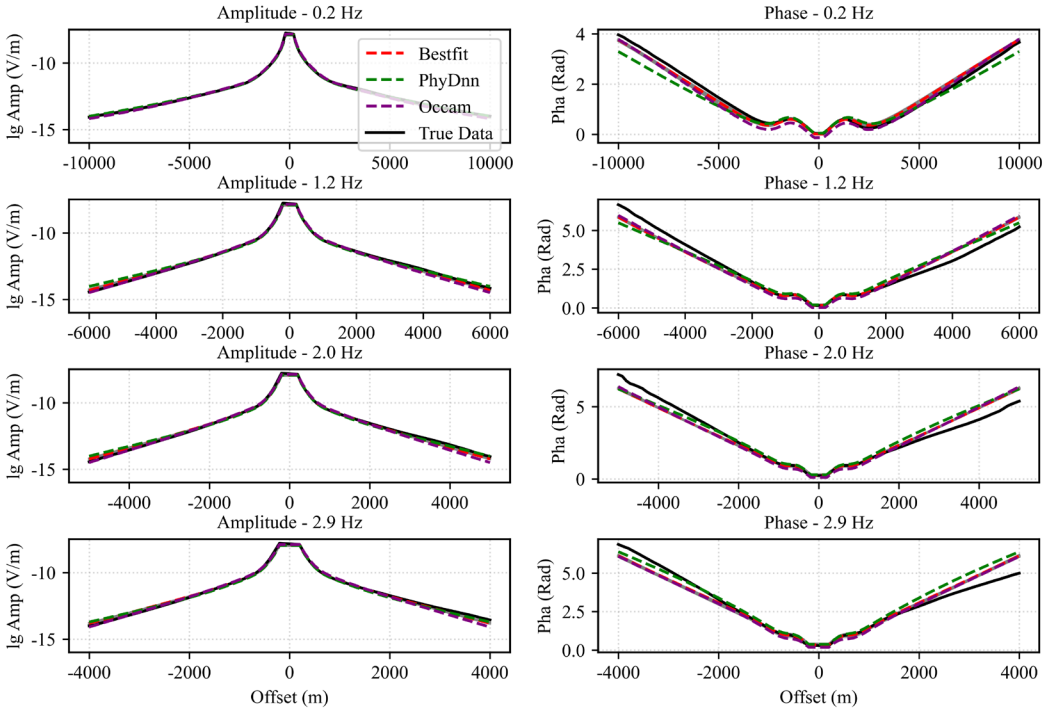



**Fig. S14** Data-fitting curves at Station P3 obtained through the perturbation prediction strategy. The black solid lines represent the data observations, the red dashed lines denote the responses corresponding to

the best-fitting model, and the gray solid lines illustrate the curves generated by individual ensemble members. The green dashed lines indicate the electromagnetic responses computed from the PhyDnn, whereas the purple dashed lines represent those yielded by the conventional Occam inversion.

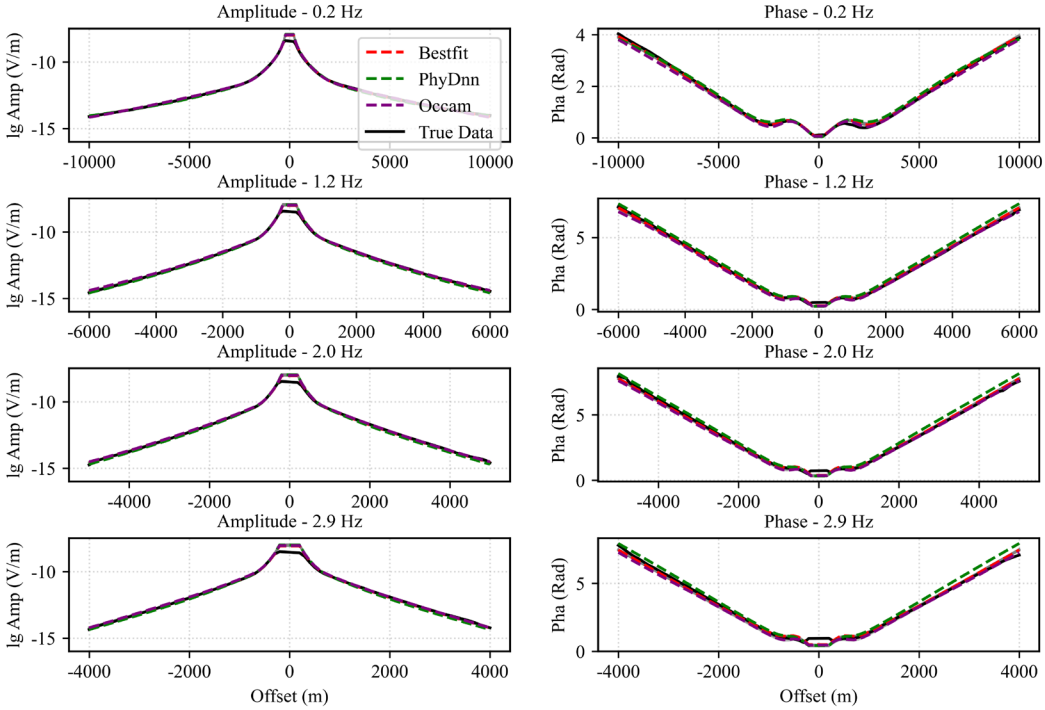



**Fig. S15** Data-fitting curves at Station P4 obtained through the perturbation prediction strategy. The black solid lines represent the data observations, the red dashed lines denote the responses corresponding to the best-fitting model, and the gray solid lines illustrate the curves generated by individual ensemble members. The green dashed lines indicate the electromagnetic responses computed from the PhyDnn, whereas the purple dashed lines represent those yielded by the conventional Occam inversion.